Monthly Notices of the ROYAL ASTRONOMICAL SOCIETY

MNRAS **528,** 6075–6098 (2024) https://doi.org/10.1093/mnras/stae313
Advance Access publication 2024 February 02

Influence of temperature on the chemical evolution and desorption of pure CO ices irradiated by cosmic-rays analogues

S. Pilling,[1]★ M. S. Mateus,[1] A. Ojeda-González,[1] L. F. A. Ferrão,[2] B. R. L. Galvão,[3] P. Boduch[4] and H. Rothard[4]

[1]*Physics and Astronomy, Instituto de Pesquisa e Desenvolvimento, Universidade do Vale do Paraíba (UNIVAP), São José dos Campos, SP, 12244-000, Brazil*
[2]*Departamento de química, Instituto Tecnológico de Aeronáutica (ITA), São José dos Campos, SP, 12228-900, Brazil*
[3]*Centro Federal de Educação Tecnológica de Minas Gerais, CEFET-MG, Av. Amazonas 5253, 30421-169, Belo Horizonte, Minas Gerais, Brazil*
[4]*GANIL – Grand Accélérateur National d'Ions Lourds Bd Henri Becquerel, Becquerel, BP 55027 – 14076, Caen, Cedex 05, France*

Accepted 2024 January 26. Received 2024 January 19; in original form 2023 September 21

ABSTRACT

Carbon monoxide (CO) plays a vital role in interstellar chemistry, existing abundantly in both gaseous and frozen environments. Understanding the radiation-driven chemistry of CO-rich ices is crucial for comprehending the formation and desorption of C-bearing molecules in the interstellar medium (ISM), particularly considering the potential impact of temperature on these processes. We report experimental data on irradiation processing of pure CO ice by cosmic ray analogues (95.2 MeV $^{136}Xe^{23+}$ ions) at temperatures of 10, 15, and 20 K, in the IGLIAS set-up coupled to the IRRSUD beamline at GANIL (Caen, France). The evolution of the irradiated frozen samples was monitored by infrared spectroscopy. The computational PROCODA code allows us to quantify the chemical evolution of the samples, determining effective reaction rates coefficients (ERCs), molecular abundances at the chemical equilibrium (CE) phase, and desorption processes. The model integrated 18 chemical species – 8 observed (CO, CO_2, C_3, O_3, C_2O, C_3O, C_3O_2, and C_5O_3) and 10 non-observed but predicted (C, O, C_2, O_2, CO_3, C_4O, C_5O, C_2O_2, C_2O_3, C_4O_2) – linked via 156 reactions. Our findings reveal temperature-driven influences on molecular abundances at chemical equilibrium, desorption yields and rates, and ERC values. Certain reaction routes exhibit distinct thermochemical behaviours of gas- and ice-phase reactions which may be attributed to the presence of neighbouring molecules within the ice matrix. This study provides pivotal insights into the chemical evolution of CO-enriched ice under irradiation, impacting solid-state astrochemistry, clarifying molecular abundances, and advancing our understanding of ISM chemistry and temperature effects on ionized radiation-processed frozen ices.

Key words: astrochemistry – molecular data – molecular processes – methods: data analysis – software: data analysis – ISM: molecules.

1. INTRODUCTION

The universal abundance of carbon monoxide (CO) and its role as a dominant carbon reservoir in molecular gas (Huang et al. 2020), establishes its significance in various interstellar environments. Beyond its presence in interstellar gas, CO is frequently detected in astrophysical ices within cold interstellar and circumstellar regions (e.g. Herbst & van Dishoeck 2009; Boogert et al. 2015). Furthermore, its identification on planetary and lunar surfaces, including Triton and Pluto, also reinforces its significant presence in cold astrophysical environments (Lellouch et al. 2010; Bertrand & Forget 2016).

The irradiation of CO-rich ices by ionizing radiation, comprising cosmic rays, UV and soft-X rays, and fast electrons, has been recognized to enhance molecular complexity in interstellar regions (e.g. Gerakines et al. 1995; Cotin et al. 2003; Jamieson et al. 2006, Palumbo et al. 2008, Domaracka et al. 2009; Pilling et al. 2010a, Seperuelo-Duarte et al. 2010; Ciaravella et al. 2012; Boduch et al. 2015; De Barros et al. 2020; de Barros et al. 2022). Recently, Gerakines et al. (2023) have also presented a review of absorption band coefficients of CO without any irradiation processes for temperatures below 30 K. The authors also calculated the optical constants for CO bands and highlight its relevance to studies of solid CO in the outer Solar System and the interstellar medium.

It is worth noting that understanding the radiation-driven chemistry of CO-rich ices is crucial for comprehending the formation and desorption of C-bearing molecules in the interstellar medium (ISM). This refers to the release of carbon-containing molecules from interstellar dust particles or ices when exposed to specific environmental conditions. This significance is magnified when we account for the potential influence of temperature on these processes.

Laboratory experiments have extensively probed the effects of ionizing radiation on CO ices at cryogenic temperatures (e.g. Gerakines et al. 1995; Jamieson et al. 2006; Seperuelo-Duarte et al. 2010; De Barros et al. 2011; Ciaravella et al. 2012, Ciaravella et al. 2016; Huang et al. 2020; Dartois et al. 2021; Gerakines et al. 2023

★ E-mail: sergiopilling@yahoo.com.br

and references therein). Notably, products such as carbon clusters (C_n), suboxide (C_3O_2), C_nO, C_nO_2, and C_nO_n species have been identified as the main outcomes of irradiated CO ices (Jamieson et al. 2006). Carbon dioxide (CO_2) has been recognized as a significant product, aligning with observations in both gas and solid phases in the ISM (Whittet et al. 1998; Gibb et al. 2004). Diatomic carbon (C_2) and other species like triatomic carbon (C_3), dicarbon monoxide (C_2O), and tricarbon monoxide (C_3O) exhibit notable presence in molecular clouds and cometary environments, further emphasizing the importance of CO ices' radiation processing (Souza & Lutz 1977; Ohishi et al. 1991; Cernicharo et al. 2000; Mookerjea et al. 2010). Palumbo et al. (2008) have postulated the potential occurrence of carbon suboxide within the ISM, stemming from the irradiation-induced processing of CO ice. This anticipation is attributed to the liberation of radiolysis products from grain surfaces to the gas phase. Indications of this species have been tentatively identified in comet Halley, as reported by Huntress et al. (1991) and Crovisier et al. (1991).

In this research, we present a dual experimental-computational study to understand the influence of temperature on irradiated pure CO ices in conditions analogous to cold space environments. The experimental data were obtained employing pure CO ices at three temperatures (10, 15, and 20 K) exposed to cosmic ray analogues (95.2 MeV $^{136}Xe^{23+}$ ions) at the GANIL (Caen, France) which supplements our previous investigation on CO irradiation at 13 K by 50 MeV $^{58}Ni^{13+}$ ions (Pilling et al. 2023a). The employed ion beam simulates the effect of super heavy mass ions cosmic rays on astrophysical ice analogues. Although the flux of such heavy ions is below 4 orders of magnitude lower than the flux of cosmic ray protons (Mennella et al. 2003; Roberts et al. 2007), their effects play an important role on interstellar grains since they can deposit much more energy (due to its high equilibrium charge state within the matter) than the light ions inside the grains. Additionally, such heavy ions also induce desorption yields during collision with solids much higher (>4 orders of magnitude higher) than promoted by light ions as in the case of protons or alphas (see also, Brown et al. 1984 and Fama et al. 2008; Seperuelo-Duarte et al. 2009a). The employed charge state of 23+ of incoming Xe ions is roughly the equilibrium charge after several collisions of such ions (independent of the initial charge state) with matter (e.g. Nastasi et al. 1996).

The computational methodology employed the PROCODA code (see also Carvalho et al. 2022; Pilling et al. 2022a, 2023a, b, c) to quantify the samples' chemical evolution, as well as to provide the effective reaction rates coefficients (ERCs) of several reactions within the and characterize the molecular abundances at the chemical equilibrium (CE) phase and desorption processes. The current model incorporated 18 chemical species – 8 observed (CO, CO_2, C_3, O_3, C_2O, C_3O, C_3O_2, and C_5O_3) and 10 non-observed but predicted (C, O, C_2, O_2, CO_3, C_4O, C_5O, C_2O_2, C_2O_3, C_4O_2) – interconnected via 156 proposed reactions (including radiation-induced destruction reactions, bimolecular reactions, and desorption reactions). The reactions proposed represent the physical and chemical processes expected within the induced liquid ice region around the energy deposition path of the ion. I t's worth noting that in the previous model, which described the chemical evolution of pure CO ice at 13 K bombarded by Ni ions (Pilling et al. 2023a), neither C_3O nor C_3O_2 was observed in the experiments (probably due to worse data quality) and belonged to the list of non-observed species.

The impact of temperature on irradiated ices was recently investigated by Pilling et al. (2023c). Utilizing the PROCODA code, the authors examined the chemical evolution of crystalline H_2O ices in the presence of 5 keV electrons, elucidating variations in ERCs, radiation induced desorption, and equilibrium abundances across ice temperatures spanning 12 to 90 K.

Section 2 describes the employed experimental and computational methodologies. The main results including details on the best-fitting models are presented in Section 3 with highlights for the temperature influence in ERCs, in molecular abundances at chemical equilibrium, and in desorption yields. This section also presents a discussion on the thermochemical behaviour disparities between gas- and ice-phase reactions that might be linked to the presence of neighbouring molecules in the ice bulk. In Section 4, we discuss the astrophysical implications of our findings and the relevance of the use of the calculated ERCs in the astrochemical models. Finally, Section 5 contains the main conclusions and closing remarks.

2. METHODOLOGY

This paper experimental infrared data obtained from irradiating CO ice with cosmic-ray analogues, along with a computational procedure utilizing the PROCODA code to map the chemical evolution of the irradiated samples. The current investigation supplements our previous work on the chemical changes observed in CO ice irradiated by cosmic rays (Pilling et al. 2023a) adding a focus on the effect of temperature in the frozen system. In the subsequent two sections, we will delve into comprehensive explanations of both methodologies employed.

2.1 The experimental data

The experimental data were obtained employing the IGLIAS (acronym for Irradiation de GLaces d'Intérêt AStrophysique) UHV chamber (Augé et al. 2018) coupled to IRRSUD beam line at GANIL (Grand Accelerateur National d'Ions Lourds) in Caen, France. Briefly, 95.2 MeV $^{136}Xe^{23+}$ ion projectiles impinge (almost perpendicularly) onto the pure CO ice target at different temperatures (10, 15, and 20 K). The chamber base pressure was around 4e-10 mbar and the projectile ion flux was around 5e8 ions cm^{-2} s^{-1}.

In-situ Fourier-transformed infrared (FTIR) spectra were recorded for ices irradiated at different fluences, up to 3e12 ions cm^{-2} using a Bruker FTIR spectrometer (Vertex 70v) with coverage from 4000 to 650 cm^{-1} and with spectral resolution of 1 cm^{-1}. A background allowing the absorbance measurements is collected before gas deposition. The total irradiation time was 6000 s for each sample. Details of the experimental setup are given in Augé et al. (2018) and also in Dartois et al. (2019, 2020).

The thin ice film was prepared by condensation of gases (purity superior to 99 per cent) onto a CsI substrate attached to a closed-cycle helium cryostat, cooled to 10 K. For all samples the deposition rates was about ∼10 μm h^{-1} and the estimated density was about 0.81 g cm^{-3} (Loeffler et al. 2005). Additionally, all samples were deposited at 10 K and heated up to the required temperature for the irradiation stage. During the entire experiment, the sample temperature remains constant and kept below the desorption temperature of CO (∼ 21 K) to avoid thermal desorption (see also Collings et al. 2004).

The irradiated area of the CsI crystal in each experiment was about 0.5 cm^2. The thicknesses of the samples were 0.54, 0.46, and 0.57 μm for the ices at 10, 15, and 20 K, respectively (see discussion at Pilling et al. 2011a and also at Dartois et al. 2020). Following Seperuelo-Duarte et al. (2010), the estimated sputtering yield (Y) for such experiments, bombarding CO ice with swift ions, was around 7e4 molecules ion^{-1}. Table 1 lists selected experimental parameters, including some sample properties and ion beam properties. Some beam properties including the max penetration depth and the linear

Table 1. Experimental parameters for the irradiation of pure CO ices by 95.2 MeV $^{136}Xe^{23+}$ ions considered in this work.

Parameter	EXP 10K	EXP 15K	EXP 20K
Sample temperature	10 K	15 K	20 K
Initial CO column density (estimated from CO band at 2139 cm^{-1}; band strength A = 1.1e-17 (Gibb et al. 2004)	9.5e17 molecules cm^{-2}	8.0e17 molecules cm^{-2}	1.0e18 molecules cm^{-2}
Sample thickness (estimated from CO band at 2139 cm^{-1}; band strength A = 1.1e-17 (Gibb et al. 2004)	0.54 μm	0.46 μm	0.57 μm
Estimated density (e.g. Loeffler et al. 2005)	0.81 g cm^{-3} = 3.48e + 22 atoms cm^{-3}		
Estimated sputtering (e.g. Seperuelo-Duarte et al. 2010)	7e4 molecules ion^{-1}		
Employed projectile	95.2 MeV $^{136}Xe^{23+}$ (0.7MeV u^{-1})		
Radiation flux	5e8 ions cm^{-2} s^{-1}		
Max penetration (SRIM calculation)	33.5 μm		
Electronic dE/dx (SRIM calculation)	1.45e3 eV/(1e15 atoms cm^{-2}) = 5e3 keV μm^{-1}		
Nuclear dE/dx (SRIM calculation)	1e1 eV/(1e15 atoms cm^{-2}) = 35 keV μm^{-1}		
Final radiation fluence	3e12 ions cm^{-2}		

energy delivered (dEdx, also known as Stopping Power) were calculated employing the SRIM code (The Stopping and Range of Ions in Matter) code. The SRIM code is a collection of software packages that calculate many features of the transport of ions in matter (Ziegler et al. 2010).

The molecular column density of a sample was determined from the relation between the optical depth $\tau_\nu = \ln(I_0/I)$ and the band strength A (cm molecules^{-1}), of the respective sample vibrational mode (see also d'Hendecourt & Allamandola 1986). In this expression, I_0 and I are the intensity of light at a specific frequency before and after passing through a sample, respectively. Since the absorbance measured by the FTIR spectrometer is $a_\nu = \log(I_0/I) = \ln(I_0/I)/\ln(10) = \tau_\nu/2.3$, the molecular column density of ice samples is provided by

$$N = \frac{1}{A}\int \tau_\nu \, d\nu \; = \frac{2.3}{A}\int a_\nu \, d\nu \;\; \left[\text{molecules cm}^{-2}\right]. \tag{1}$$

In this paper, eight species (CO, C_3, C_2O, CO_2, O_3, C_3O, C_3O_2, and C_5O_2) were identified and quantified in the experimental data. The vibrational band positions and their infrared absorption coefficients (band strengths) used in this work are given in Table 2. Once more, it's important to highlight that in the previous model, where the chemical evolution of pure CO ice was studied at 13 K under bombardment by Ni ions (Pilling et al. 2023a), both C_3O and C_3O_2 were not detected in experiments, being only in the list of non-observed species. In this work, we are able to measure and model these two species in irradiated ice. A comparison between selected ion properties of Xe and Ni ions (and also of protons and Fe ions) are presented and discussed in the Appendix A.

2.2 The PROCODA code

The PROCODA code (acronym for PROgram for solving Couple Differential equations set for Astrochemistry), elaborated upon in Pilling et al. (2022a), aims to solve a set of interconnected differential equations to depict the chemical evolution of typical astrophysical ices over time when exposed to ionizing radiation processing. This approach is further elucidated in Carvalho et al. (2022) and improved to consider thermochemistry data associated with the species under consideration (Pilling et al. 2023a, b). The code provides numerical values for the effective rate coefficients (ERCs), also known as rate constants (k) in case of gas-phase reactions, the molecular abundances of both observed and non-observed (but predicted) species, and essential information for the radiation induced desorption to the gas-phase. While the proposed reactions represent the physical and chemical processes that are expected to occur within the ice, they are not necessarily elementary reactions. As a result, their rate constants (or coefficients) are referred to as effective (apparent). Each effective reaction's rate also considers the availability of involved reactants (N_i) up to the second order. Details of the current code version can be obtained at Pilling et al. (2023a, b).

Briefly, the typical equation in the chemically coupled system solved by the code has the following parameters:

$$\frac{dN_i}{dt} = \left[-DES_i(t) \; - \sum_{d1} k_{d1} N_i(t) - \sum_{d2} k_{d2} N_i(t) N_a(t)/L\right] + \left[\sum_{p1} k_{p1} N_a(t) + \sum_{p2} k_{p2} N_a(t) N_b(t)/L\right] \left[\text{molecules cm}^{-2}\,\text{s}^{-1}\right] \tag{2}$$

where N_i is the column density of given species i, in units of molecules cm^{-2}, dN_i/dt is its column density variation along the time t, k values are the ERCs for the different reactions and L indicates the sample average thickness in units of cm. The values $k_{d1}$and k_{d2} indicate the destruction (consumption) processes and values $k_{p1}$and k_{p2} indicate the production processes of a given species i, in direct and bimolecular radiation-induced reactions. The rates k_{d1} and k_{p1} represent the direct dissociation reactions induced by radiation and have units of s^{-1} and the rates $k_{d2}$and k_{p2} represent the bimolecular collision reactions induced by radiation, in units of cm^3 molecules^{-1} s^{-1}. In this equation the $DES_i(t) = k_{des,i}\ \Omega_i(t)\ N_i(t)$ is the differential column density estimation due to desorption, i.e. the number of molecules (or atomic species) that desorbs from ice to gas-phase per cm^2 and per second due to incoming radiation, which also depends on the intrinsic desorption rate ($k_{des,i}$), in units of s^{-1}, and the dimension-less surface coverage of the species i as a function of time ($\Omega_i(t)$). The values $N_a$and N_b indicate the column densities of species a and b, in units of molecules cm^{-2}, respectively, which participate in the reaction to produce or consume the respective i species. The list with the full employed equations was presented in appendix B section of Pilling et al. (2023a).

As discussed by Pilling et al. (2023a), who also investigated the chemical evolution of CO ice under processing by incoming cosmic-ray analogues employing the PROCODA code, the considered score function (SF) employed in the minimization algorithm during the

Table 2. Infrared absorption coefficients (band strengths) used in the column density calculations for the observed molecules.

Wavenumber (cm^{-1})	Wavelength (μm)	Molecular assignment	Band strength (A) (cm $molecule^{-1}$)	Refs.
2342	4.27	CO_2 (v3)	7.6e-17	Gerakines et al. (1995)
2249	4.45	C_3O	1e-17*	Palumbo et al. (2008)
2242	4.46	C_3O_2	13e-17	Gerakines & Moore (2001)
2139	4.67	CO (v1)	1.1e-17	Gibb et al. (2004)
2060	4.85	C_5O_2	7.4e-17	Jamieson et al. (2006)
2019	4.95	C_3	1.3e-16	Jamieson et al. (2006)
1989	5.03	C_2O	2.4e-17	Jamieson et al. (2006)
1041	9.61	O_3	1.53e-17	Bennett & Kaiser (2005)

*considered.

search for the best solution of coupled chemical systems was

$$\begin{aligned}
\mathrm{SF} = {} & p1 \times \sum \frac{(\mathrm{oCO_{data}} - \mathrm{oCO_{data}})^2}{\mathrm{oCO_{data}}} + \\
& p2 \times \sum \frac{(\mathrm{oCO2_{data}} - \mathrm{oCO2_{model}})^2}{\mathrm{oCO2_{data}}} + \\
& p3 \times \sum \frac{(\mathrm{oC3_{data}} - \mathrm{oC3_{model}})^2}{\mathrm{oC3_{data}}} + \\
& p4 \times \sum \frac{(\mathrm{oO3_{data}} - \mathrm{oO3_{model}})^2}{\mathrm{oO3_{data}}} + \\
& p5 \times \sum \frac{(\mathrm{oC2O_{data}} - \mathrm{oC2O_{model}})^2}{\mathrm{oC2O_{data}}} + \\
& p6 \times \sum \frac{(\mathrm{oC3O_{data}} - \mathrm{oC3O_{model}})^2}{\mathrm{oC3O_{data}}} + \\
& p7 \times \sum \frac{(\mathrm{oC3O2_{data}} - \mathrm{oC3O2_{model}})^2}{\mathrm{oC3O2_{data}}} + \\
& p8 \times \sum \frac{(\mathrm{oC5O2_{data}} - \mathrm{oC5O2_{model}})^2}{\mathrm{oC5O2_{data}}} + \\
& p9 \times [(1 - \mathrm{MSC_f}) + (1 - \mathrm{MSCo_f}) + (1 - \mathrm{MSCo_m})] + \\
& p10 \times (1 - \mathrm{DSC}) + p11 \times (1 - \mathrm{SSC}), \qquad (3)
\end{aligned}$$

where the dimension-less parameters $p1$ to $p11$ in this equation are the weights of each term, used as a tool to search for the best solution during the computational minimization processes. In this equation, the $\mathrm{o[]_{data}}$ and $\mathrm{o[]_{model}}$ are the column density values of given observed species taken from the experimental interpolated data and their respective value calculated by the model, respectively. The parameter $\mathrm{MSC_f}$ is the model mass similarity criterion (or model mass conservation), calculated considering the similarity between the initial column mass of the modelled system and the total column mass of the model at the final modelling time (at largest time) (including both masses, at the ice and desorbed), $\mathrm{MSCo_f}$ and $\mathrm{MSCo_m}$ are the column mass similarity criterion between the experimentally observed column mass and the observed column mass in the model at the final modelling time and at the middle of the modelling time, respectively. From these three parameters, we calculate a parameter called 'mass similarity criterion' MSC = ($\mathrm{MSC_f}$ × 100 per cent + $\mathrm{MSCo_f}$ × 100 per cent + $\mathrm{MSCo_m}$ × 100 per cent)/3, which also helps us to indicate how good the solution of the system is compared with the observed data. The parameter DSC is the 'desorption similarity criterion', calculated considering the similarity between the experimental desorption yield (estimated from the experimental employed manuscript or other similar experimental data) and the total molecular desorption yield computed by the model. The parameter SSC is the 'slope similarity criterion', which is related to the achievement of CE phase in the ice at larger radiation fluence, as described in Pilling et al. (2022a).

It is worth noting that the chi-squared function χ^2 (also named summed CHI2) can be obtained directly from equation (3) making $p1 = p2 = p3 = p4 = p5 = p6 = p7 = p8 = 1$ and $p9 = p10 = p11 = 0$. The chi-squared function is a parameter obtained considering the experimental column density of the observed molecules (CO, CO_2, C_3, O_3, C_2O, C_3O, C_3O_2, and C_5O_3) and their modelled column density by the code.

As presented by Piling et al. (2023a), the employed chemical network considered a total of 156 coupled equations describing the chemical evolution of selected molecules in pure CO ices under the presence of different ionizing radiation types (including direct and bimolecular reactions). The reaction set also includes 18 radiation-induced molecular desorption to take into account the frozen species that are ejected to the gas-phase during the irradiation. The proposed reaction network involves 18 different chemical species within the ice (8 observed species from experiments: CO, CO_2, C_3, O_3, C_2O, C_3O, C_3O_2, and C_5O_3; 10 non-observed species: C, O, C_2, O_2, CO_3, C_4O, C_5O, C_2O_2, C_2O_3, and C_4O_2).

The thermochemistry info for the considered species is given in Pilling et al. (2023a) and the extensive discussion on the code advantages, uncertainties, and limitations, is provided by Pilling et al. (2022a, 2023a, b). The model uncertainties are below 20 per cent (see discussion at Pilling et al. 2022a).

3. RESULTS AND DISCUSSION

3.1 Column density measurements from the evolution of ice spectra

Fig. 1 presents the changes observed in the infrared spectrum of pure CO ice at 20 K during bombardment by cosmic rays (95.2 MeV $^{136}Xe^{23+}$ ions). The main panel presents the entire spectra obtained at four radiation fluences (0, 1.6e11, 1.3e12, and 3e12 ions cm^{-2}). The inset panels show details of the spectra with the peak position of the observed and quantified species indicated. Similar data were also collected for pure CO ice at 10 and 15 K (not shown). It is worth noting that the CO band presents a peculiar profile (probably due to spectrometer background subtraction processes) which could slightly increase the uncertainty in its quantification. To minimize this effect we also considered the data of the ^{13}CO band at 2092 cm^{-1} (A = 1.3e-17 cm $molecule^{-1}$, see also Gerakines et al. 1995). For details on the peak assignments and other species possibly presented in the ice see also de Barros et al. (2011).

The evolution of column density (normalized to CO initial column density) of observed species during the irradiation of pure CO ices at three different temperatures (10, 15, and 20 K) irradiated by cosmic rays (95.2 MeV $^{136}Xe^{23+}$ ions) up to the fluence of 3e12 ions cm^{-2} is shown in Fig. 2. Eight molecular species were observed and

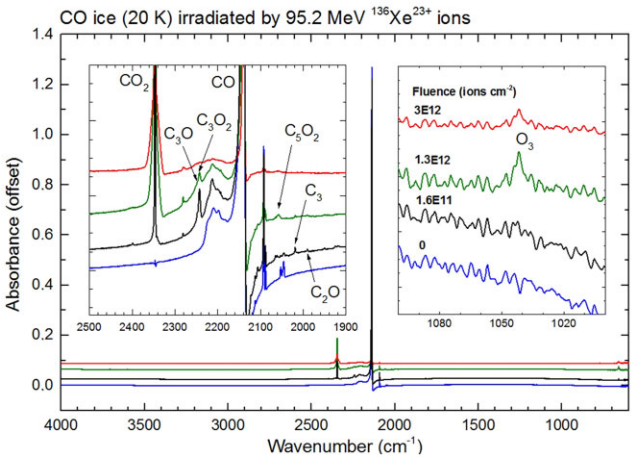

Figure 1. Evolution of infrared spectrum of CO ice at 20 K irradiated by 95.2 MeV $^{136}Xe^{23+}$ ions) up to the fluence of 3e12 ions cm^{-2}. Spectra colour code: blue (bottommost) = unirradiated spectrum; black = spectrum recorded at the fluence of 1.6e11 ions cm^{-2}; green = spectrum recorded at the fluence of 1.3e12 ions cm^{-2} and red (topmost) = spectrum recorded at the fluence of 3e12 ions cm^{-2}. The attribution of some infrared bands is indicated. See details in the text.

quantified by IR spectroscopy (CO, CO_2, C_3, O_3, C_2O, C_3O, C_3O_2, and C_5O_2). The column density of CO (parent species) shows a decrement trend with increasing fluence, exhibiting a more rapid decrease at lower temperatures. In contrast, all other species under study (daughter species) demonstrated an accelerated formation rate in the initial stages of irradiation, culminating in a peak in column density, followed by a subsequent decrease as the fluence continued to increase.

It's important to highlight that the amount of CO, CO_2, and C_3O_2, seems to increase with the temperature (see Fig. 2a). For the other observed species a peculiar relation between column density evolution and the temperature of irradiated ice (non-clear dependence with the ice´s temperature). It is worth noting that the daughters species C_3O and C_3O_2, detected in this study, were not detected (probably due to a lower data quality) in similar experiment performed by Seperuelo-Duarte et al. (2010) employed Ni ion in pure CO ice at 13 K and modelled previously with PROCODA (Pilling et al. 2023a). The experimental error was estimated to be below 20 per cent.

3.2 Chemical evolution at different temperatures mapped via PROCODA code

Fig. 3 illustrates the evolution of column density for the most accurate models employing the PROCODA code on pure CO ices irradiated by cosmic-ray analogues (95.2 MeV $^{136}Xe^{23+}$ ions) at three different temperatures studied. Panels a, b, and c, present the results for the temperatures of 10, 15, 20 K, respectively. The symbols represent the experimental data. The bold-dashed blue line represents the modelled summed desorption column density. Important model output parameters are displayed in the header.

The model reveals a remarkable match between experimental data and the best-fitting model for most species, with an exception for C_5O_2. As discussed by Pilling et al. (2023a), the current model suggests much smaller abundances for C_5O_2 than the observed values in the experiments and the possible explanation for this issue are: (i) lack of important reaction to describe the chemical evolution of this species and (ii) an overestimation in the abundance of this species from the experimental work. From the chemical point of view, the production of C_5O_2 requires at least five molecules of CO or collisions between other carbon containing species, such as C_3O_2 or C_3. In the case of C_3O_2, the model encounters challenges in fitting experimental data during the initial stages of irradiation. This difficulty may be attributed to the occurrence of chemical reactions between CO and its radiation-induced daughters and granddaughters species (which may also include ionic species) which were not accounted for in the current reaction set. However, at larger fluences, and at chemical equilibrium (CE) phase, the models reveal a good match with the experimental data.

In all models, atomic O and C were the most produced species, followed by CO_2, O_2, and C_2.

3.3 Temperature influence on ERCs

The primary findings for the best-fitting models, utilizing the PROCODA code on pure CO ices at different temperatures exposed to 95.2 MeV $^{136}Xe^{23+}$ ions, are presented in Table 3. The listed values encompass the calculated ERCs (named as 'k value') and the branching ratio [named as BR(per cent)] for the relevant reaction groups obtained at different temperatures. The table also presents the reactions considered in the model and the enthalpy of reaction ($\Delta_R H$) in the gas-phase (at 0 Kelvin, considering the lowest formation enthalpy for each species), employed in phase 1 calculations as discussed previously. The parameter 'k label' specifies whether the reaction belongs to a group (indicating also the other members of this group), is a single reaction, or pertains to desorption. The estimation of the error in rate coefficients suggests it to be below 20 per cent, as discussed by Pilling et al. (2022a, 2023a, b). Once more, we would like to explicitly state that, we can consider the ERCs as total reaction rate coefficients that may include a multitude of processes, especially since ions and excitations are not incorporated in the model.

Table 4 presents the average values for the ERCs and desorption obtained by the best-fitting model considered in the mapping of the chemical evolution of pure CO ice irradiated by cosmic rays (employing 95.2 MeV $^{136}Xe^{23+}$ ions) at different temperatures (10 K, 15 K, and 20 K). A comparison with the average values obtained for pure CO ices irradiated by 50 MeV Ni ions obtained by using a similar methodology (Pilling et al. 2023a) was also listed for comparison purposes. The calculated values between this work and the previous one (Pilling et al. 2023a) present good similarity showing that current average ERCs values at 10 K are lower than the obtained employing 50 MeV Ni ions at 13 K. Additionally, as expected, the radiation-induced desorption yield in this paper was larger than the value obtained by Pilling et al. (2023a), respecting the fact that Xe ions have a slight larger electronic stopping power than Ni ions with equivalent energy/mass ratio (see also Appendix A).

The average values for the ERCs in a graphical way to better visualization of data tendencies are presented in Fig. 4. We observe that average values of ERCs for intrinsic desorption have largely increased with the temperature among the studied range between 10 and 20 K. The largest changes were observed when comparing the ERCs of intrinsic desorption at 20 K (∼6 times higher) with respect to the value at 15 K which might be associated with the fact that this higher temperature is close to the CO desorption temperature (∼ 21 K; Collings et al. 2004). In the case of direct dissociation collision reactions, we observed a very small increase in the temperature. No clear dependence with temperature was observed for the bimolecular ERCs among the models errors.

Changes in the ERCs for several reactions in crystalline water ices, irradiated by 5 keV electrons, were also quantified and discussed

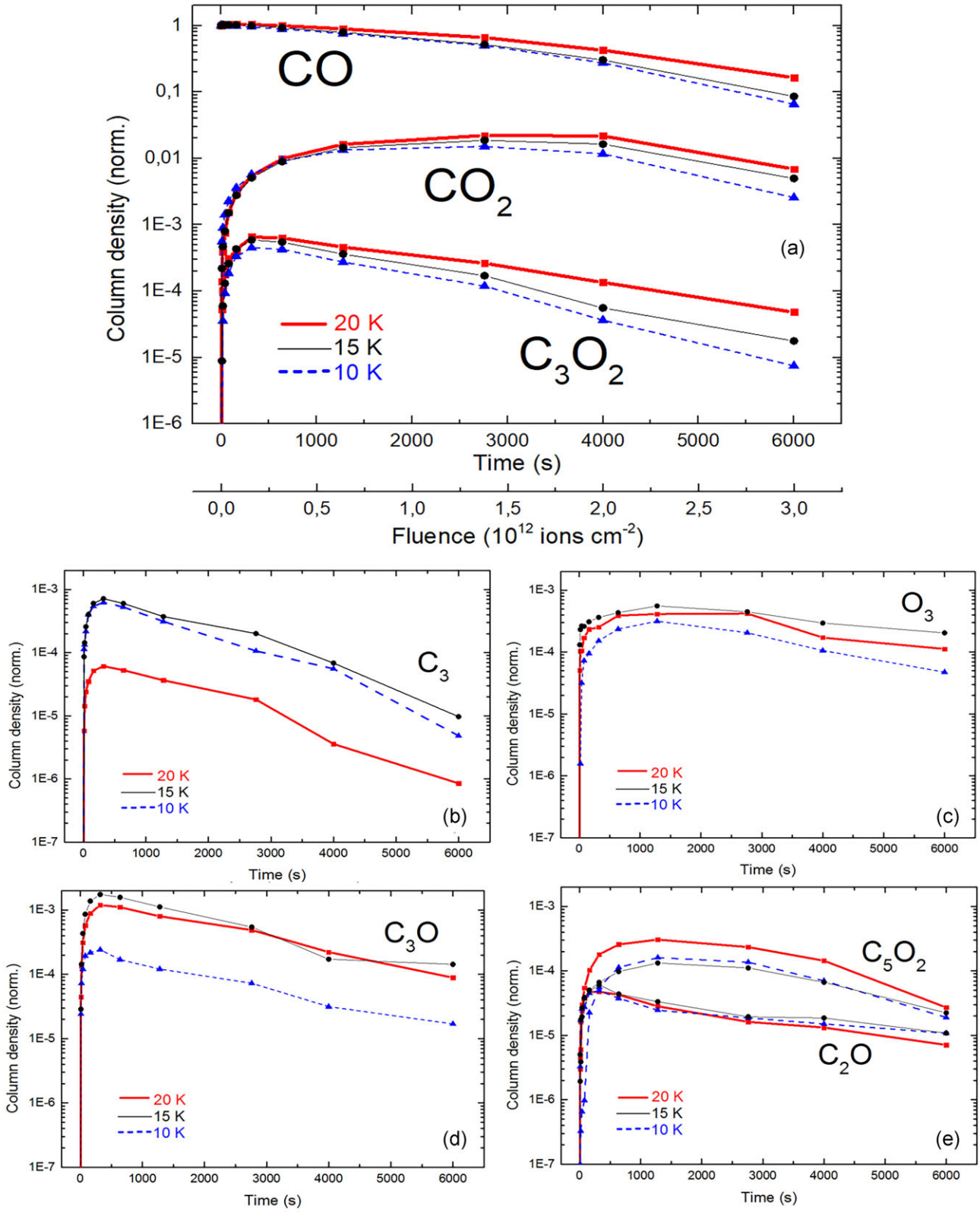

Figure 2. Column density evolution (normalized by CO initial column density) as a function of irradiation time pure CO ices at three different temperatures (10, 15, and 20 K) irradiated by cosmic rays (95.2 MeV $^{136}Xe^{23+}$ ions) up to fluence of 3e12 ions cm^{-2}. The experimental error was estimated to be below 20 per cent.

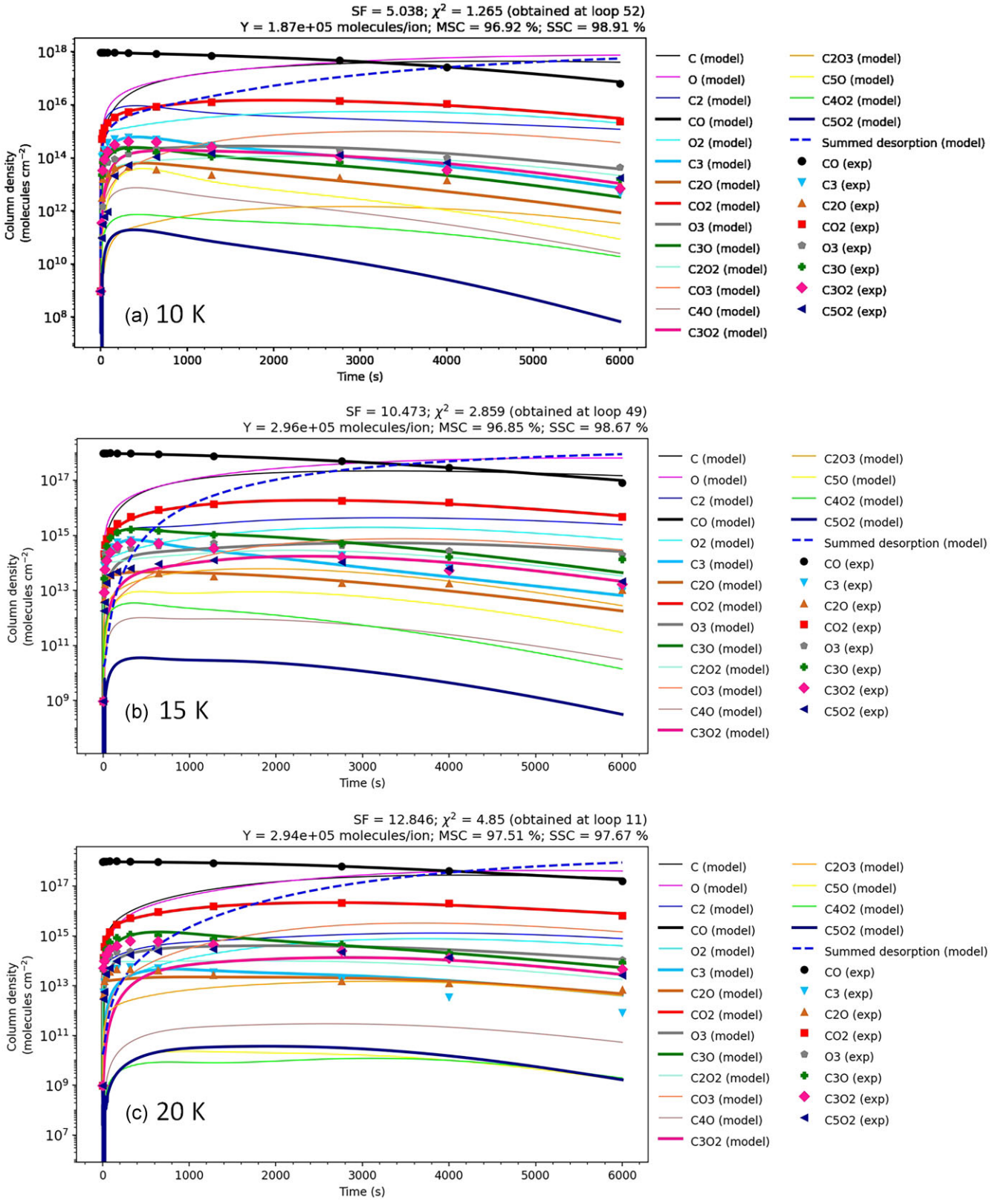

Figure 3. The evolution of column density obtained for the best-fitting model employing the PROCODA code on Pure CO ices irradiated by cosmic rays (95.2 MeV $^{136}Xe^{23+}$ ions) at different temperatures. Panels a, b, and c present the results for the temperatures of 10, 15, 20 K, respectively. The coloured symbols represent the experimental data. The bold-dashed blue line represents the modelled summed desorption column density at a given time (proportional to the amount of molecules that goes to gas-phase during ice irradiation). Important model output parameters are displayed in the header including the total desorption yield (Y) in units of molecules/ion. The experimental error and model uncertainties was estimated to be below 20 per cent. See details in the text.

Table 3. Reactions considered in the mapping of chemical evolution of pure CO ices irradiated by cosmic rays (95.2 MeV $^{136}Xe^{23+}$ ions) at different temperatures and the main outcomes from the best-fitting models, including the ERCs (k values) and the branching ratio [BR(per cent)] of reactions within the considered reaction groups. The ERCs and BR(per cent) values obtained by Pilling et al. (2023a), considering similar methodology on pure CO ice irradiated by 50 MeV Ni ions at 13 K are also listed for comparison purposes. See details in the text.

Reactions parameters						10 K (this wok)		13 K irradiated by 50 MeV Ni ions (Pilling et al. 2023a)		15 K (this wok)		20 K (this wok)	
Reaction label	Reactants	Products	$\Delta_r H$	k label**	k unit	k value	BR (per cent)	k value	BR(per cent)	k value	BR (per cent)	k value	BR (per cent)
r1	CO2 + RAD*	O + CO	526.15	k1 (G26; [k1, k3])	s^{-1}	1.32e-03	99.78	1.45e-03	86.93	1.43e-02	99.45	4.60e-03	~100
r2	O + CO	CO2	-526.15	k2 (G30; [k2, k57])	cm^3 $molecules^{-1}$ s^{-1}	4.21e-26	33.63	7.40e-26	53.62	1.05e-25	59.49	8.31e-26	56.84
r3	CO2 + RAD	C + O2	1104.5	k3 (G26; [k1, k3])	s^{-1}	2.88e-06	0.22	2.18e-04	13.07	7.90e-05	0.55	≤1.0e-08	~0
r4	C + O2	CO2	-1104.5	k4 (G5; [k4, k58])	cm^3 $molecules^{-1}$ s^{-1}	2.35e-25	98.31	3.04e-25	98.21	2.37e-25	77.83	1.90e-25	31.00
r5	CO2 + CO2	O2 + C2O2	801.12	k5 (G25; [k9, k7, k5])	cm^3 $molecules^{-1}$ s^{-1}	3.09e-25	14.72	1.31e-25	26.31	5.35e-25	27.76	1.29e-26	0.72
r6	O2 + C2O2	CO2 + CO2	-801.12	k6 (single)	cm^3 $molecules^{-1}$ s^{-1}	5.66e-24	100	1.75e-23	100	1.65e-24	100	3.30e-23	100
r7	CO2 + CO2	O + C2O3	750.86	k7 (G25; [k9, k7, k5])	cm^3 $molecules^{-1}$ s^{-1}	2.30e-25	10.96	1.80e-25	36.14	1.03e-24	53.45	1.07e-25	5.98
r8	O + C2O3	CO2 + CO2	-750.86	k8 (single)	cm^3 $molecules^{-1}$ s^{-1}	2.77e-25	100	1.02e-23	100	1.27e-23	100	3.14e-24	100
r9	CO2 + CO2	CO + CO3	545.49	k9 (G25; [k9, k7, k5])	cm^3 $molecules^{-1}$ s^{-1}	1.56e-24	74.32	1.87e-25	37.55	3.62e-25	18.79	1.67e-24	93.30
r10	CO + CO3	CO2 + CO2	-545.49	k10 (single)	cm^3 $molecules^{-1}$ s^{-1}	7.45e-26	100	1.03e-25	100	8.45e-26	100	3.19e-26	100
r11	O + CO2	CO + O2	32.47	k11 (G31; [k15, k11, k13])	cm^3 $molecules^{-1}$ s^{-1}	5.98e-25	12.94	1.24e-25	9.57	6.64e-25	24.35	6.82e-25	21.00
r12	CO + O2	O + CO2	-32.47	k12 (G23; [k12, k65, k63])	cm^3 $molecules^{-1}$ s^{-1}	3.45e-25	75.41	3.08e-25	85.34	3.19e-25	51.34	2.55e-25	52.85
r13	O + CO2	C + O3	1002.05	k13 (G31; [k15, k11, k13])	cm^3 $molecules^{-1}$ s^{-1}	1.95e-25	4.22	1.39e-27	0.11	2.73e-25	10.01	4.62e-26	1.42
r14	C + O3	O + CO2	-1002.05	k14 (G6; [k14, k64])	cm^3 $molecules^{-1}$ s^{-1}	4.45e-23	94.06	7.67e-24	51.86	7.33e-24	35.88	1.07e-23	98.81
r15	O + CO2	CO3	19.34	k15 (G31; [k15, k11, k13])	cm^3 $molecules^{-1}$ s^{-1}	3.83e-24	82.85	1.17e-24	90.32	1.79e-24	65.64	2.52e-24	77.58
r16	CO3 + RAD	O + CO2	-19.34	k16 (G27; [k16, k66])	s^{-1}	4.32e-01	98.96	2.44e-01	98.2	3.63e-01	99.45	7.48e-02	74.21
r17	O2 + CO2	CO + O3	423.7	k17 (G34; [k17, k19])	cm^3 $molecules^{-1}$ s^{-1}	3.63e-23	85.25	2.88e-23	68.25	4.13e-24	53.08	3.56e-23	44.95
r18	CO + O3	O2 + CO2	-423.7	k18 (G24; [k18, k67])	cm^3 $molecules^{-1}$ s^{-1}	2.01e-25	70.87	7.30e-26	75.65	7.48e-26	62.28	7.76e-26	76.53
r19	O2 + CO2	O + CO3	513.02	k19 (G34; [k17, k19])	cm^3 $molecules^{-1}$ s^{-1}	6.28e-24	14.75	1.34e-23	31.75	3.65e-24	46.92	4.36e-23	55.05
r20	O + CO3	O2 + CO2	-513.02	k20 (G32; [k20, k68])	cm^3 $molecules^{-1}$ s^{-1}	2.03e-26	59.18	1.25e-26	83.78	1.82e-25	78.96	6.81e-26	97.27
r21	C + CO2	C2 + O2	502.05	k21 (G4; [k23, k25, k21])	cm^3 $molecules^{-1}$ s^{-1}	4.45e-26	5.11	6.21e-27	0.62	7.64e-27	0.92	5.09e-27	2.17
r22	C2 + O2	C + CO2	-502.05	k22 (G9; [k50, k98, k22])	cm^3 $molecules^{-1}$ s^{-1}	1.26e-24	1.85	3.93e-25	0.75	1.97e-25	0.51	1.42e-24	4.75
r23	C + CO2	CO + CO	-545.88	k23 (G4; [k23, k25, k21])	cm^3 $molecules^{-1}$ s^{-1}	1.41e-25	16.18	5.08e-25	50.99	3.12e-25	37.43	1.23e-25	52.32
r24	CO + CO	C + CO2	545.88	k24 (G21; [k47, k24, k51, k49])	cm^3 $molecules^{-1}$ s^{-1}	8.54e-28	14.66	1.85e-28	4.72	2.54e-28	5.94	7.60e-30	0.28
r25	C + CO2	C2O2	-303.38	k25 (G4; [k23, k25, k21])	cm^3 $molecules^{-1}$ s^{-1}	6.86e-25	78.71	4.82e-25	48.38	5.14e-25	61.66	1.07e-25	45.51
r26	C2O2 + RAD	C + CO2	303.38	k26 (G12; [k48, k26, k95, k97])	s^{-1}	1.77e-01	20.15	2.28e-01	21.71	1.07e-01	27.34	2.07e-01	48.26
r27	CO + CO2	C2O3	224.71	k27 (G22; [k27, k29, k31, k33])	cm^3 $molecules^{-1}$ s^{-1}	≤5.7e-31	25.00	4.56e-26	35.05	2.69e-25	80.37	2.91e-26	37.12
r28	C2O3 + RAD	CO + CO2	-224.71	k28 (G13; [k28, k75, k77, k99, k101])	s^{-1}	8.31e-01	55.29	5.96e-01	36.43	7.51e-01	75.65	4.89e-01	53.56
r29	CO + CO2	O + C2O2	768.65	k29 (G22; [k27, k29, k31, k33])	cm^3 $molecules^{-1}$ s^{-1}	≤5.7e-31	25.00	3.72e-26	28.59	1.83e-26	5.47	≤5.7e-31	0
r30	O + C2O2	CO + CO2	-768.65	k30 (G29; [k30, k76])	cm^3 $molecules^{-1}$ s^{-1}	1.59e-24	52.48	6.76e-24	89.32	2.93e-24	89.66	5.95e-24	97.97
r31	CO + CO2	O2 + C2O	884.03	k31 (G22; [k27, k29, k31, k33])	cm^3 $molecules^{-1}$ s^{-1}	<5.7e-31	25.00	2.43e-26	18.68	≤5.7e-31	0	<5.7e-31	0
r32	O2 + C2O	CO + CO2	-884.03	k32 (G33; [k32, k78])	cm^3 $molecules^{-1}$ s^{-1}	1.75e-23	82.39	4.92e-23	53.83	2.84e-23	89.62	7.63e-24	71.38
r33	CO + CO2	C2 + O3	1471.63	k33 (G22; [k27, k29, k31, k33])	cm^3 $molecules^{-1}$ s^{-1}	<5.7e-31	25.00	2.30e-26	17.68	4.74e-26	14.16	4.93e-26	62.88
r34	C2 + O3	CO + CO2	-1471.63	k34 (G10; [k34, k102])	cm^3 $molecules^{-1}$ s^{-1}	1.31e-23	83.76	4.15e-23	88.45	5.56e-24	69.33	4.78e-23	90.10
r35	C2O + CO2	CO + C2O2	-82.91	k35 (G11; [k35, k37])	cm^3 $molecules^{-1}$ s^{-1}	2.82e-24	83.28	7.26e-25	50.88	2.73e-24	74.63	2.22e-24	63.07
r36	CO + C2O2	C2O + CO2	82.91	k36 (single)	cm^3 $molecules^{-1}$ s^{-1}	1.73e-25	100	4.11e-26	100	2.14e-25	100	3.40e-25	100
r37	C2O + CO2	C + C2O3	445.18	k37 (G11; [k35, k37])	cm^3 $molecules^{-1}$ s^{-1}	5.66e-25	16.72	7.01e-25	49.12	9.28e-25	25.37	1.30e-24	36.93
r38	C + C2O3	C2O + CO2	-445.18	k38 (single)	cm^3 $molecules^{-1}$ s^{-1}	4.71e-26	100	3.34e-26	100	6.30e-26	100	2.67e-25	100
r39	C2 + CO2	CO + C2O	-163.9	k39 (G8; [k90, k39, k41])	cm^3 $molecules^{-1}$ s^{-1}	8.79e-24	14.87	1.69e-24	23.76	1.69e-24	36.79	2.70e-24	42.12
r40	CO + C2O	C2 + CO2	163.9	k40 (G20; [k40, k61])	cm^3 $molecules^{-1}$ s^{-1}	4.55e-24	85.95	2.59e-24	60.66	2.33e-24	66.76	1.98e-23	94.65
r41	C2 + CO2	C + C2O2	299.07	k41 (G8; [k90, k39, k41])	cm^3 $molecules^{-1}$ s^{-1}	2.54e-24	4.30	7.02e-25	9.87	5.74e-25	12.49	2.56e-24	39.94
r42	C + C2O2	C2 + CO2	-299.07	k42 (G2; [k88, k62, k42])	cm^3 $molecules^{-1}$ s^{-1}	3.42e-26	6.45	1.20e-25	12.61	8.32e-26	3.27	1.98e-25	4.10
r43	CO2 + O3	O2 + CO3	121.79	k43 (single)	cm^3 $molecules^{-1}$ s^{-1}	9.52e-24	100	6.79e-24	100	1.24e-24	100	2.89e-23	100

Table 3 – *continued*

Reaction label	Reactions parameters					10 K (this wok)		13 K irradiated by 50 MeV Ni ions (Pilling et al. 2023a)		15 K (this wok)		20 K (this wok)	
	Reactants	Products	$\Delta_r H$	k label**	k unit	k value	BR (per cent)	k value	BR(per cent)	k value	BR (per cent)	k value	BR (per cent)
r44	O2 + CO3	CO2 + O3	-121.79	k44 (single)	cm^3 $molecules^{-1}$ s^{-1}	1.47e-26	100	6.28e-27	100	1.63e-25	100	2.86e-25	100
r45	CO + RAD	C + O	1072.03	k45 (single)	s^{-1}	≤1.0e-08	100	≤ 1.0e-08	100	≤1.0e-08	100	≤1.0e-08	100
r46	C + O	CO	-1072.03	k46 (single)	cm^3 $molecules^{-1}$ s^{-1}	<5.7e-31	100	≤5.9e-31	100	≤5.7e-31	100	≤5.7e-31	100
r47	CO + CO	C2O2	242.5	k47 (G21; [k47, k24, k51, k49])	cm^3 $molecules^{-1}$ s^{-1}	1.49e-27	25.58	2.57e-27	65.63	2.38e-27	55.71	2.34e-27	86.79
r48	C2O2 + RAD	CO + CO	-242.5	k48 (G12; [k48, k26, k95, k97])	s^{-1}	6.95e-01	79.12	8.11e-01	77.21	2.80e-01	71.54	2.20e-01	51.29
r49	CO + CO	C2 + O2	1047.93	k49 (G21; [k47, k24, k51, k49])	cm^3 $molecules^{-1}$ s^{-1}	3.48e-27	59.75	8.15e-28	20.81	1.56e-27	36.51	≤5.7e-31	0.02
r50	C2 + O2	CO + CO	-1047.93	k50 (G9; [k50, k98, k22])	cm^3 $molecules^{-1}$ s^{-1}	2.56e-23	37.56	3.63e-23	69.28	3.75e-23	96.61	2.51e-23	83.97
r51	CO + CO	O + C2O	851.56	k51 (G21; [k47, k24, k51, k49])	cm^3 $molecules^{-1}$ s^{-1}	5.68e-31	0.01	3.46e-28	8.84	7.85e-29	1.84	3.48e-28	12.91
r52	O + C2O	CO + CO	-851.56	k52 (G28; [k52, k96])	cm^3 $molecules^{-1}$ s^{-1}	3.57e-23	49.45	4.70e-23	61.6	4.36e-23	79.27	1.87e-23	95.30
r53	C + CO	C2O	-220.47	k53 (G3; [k53, k55])	cm^3 $molecules^{-1}$ s^{-1}	≤5.7e-31	0.01	1.08e-26	99.99	1.81e-27	35.28	≤5.7e-31	0.05
r54	C2O + RAD	C + CO	220.47	k54 (single)	s^{-1}	2.04e-02	100	3.48e-02	100	1.43e-02	100	7.76e-02	100
r55	C + CO	O + C2	469.58	k55 (G3; [k53, k55])	cm^3 $molecules^{-1}$ s^{-1}	9.26e-27	99.99	≤5.9e-31	0.01	3.32e-27	64.72	1.15e-27	99.95
r56	O + C2	C + CO	-469.58	k56 (single)	cm^3 $molecules^{-1}$ s^{-1}	4.56e-26	100	5.97e-26	100	3.58e-25	100	2.70e-26	100
r57	O + CO	C + O2	578.35	k57 (G30; [k2, k57])	cm^3 $molecules^{-1}$ s^{-1}	8.31e-26	66.37	6.40e-26	46.38	7.15e-26	40.51	6.31e-26	43.16
r58	C + O2	O + CO	-578.35	k58 (G5; [k4, k58])	cm^3 $molecules^{-1}$ s^{-1}	4.05e-27	1.69	5.54e-27	1.79	6.75e-26	22.17	4.23e-25	69.00
r59	C2 + CO	C + C2O	381.98	k59 (G7; [k84, k59])	cm^3 $molecules^{-1}$ s^{-1}	<5.68e-31	∼0	3.40e-26	17.89	3.06e-26	1.03	2.10e-25	6.21
r60	C + C2O	C2 + CO	-381.98	k60 (G1; [k82, k60])	cm^3 $molecules^{-1}$ s^{-1}	1.44e-25	83.19	4.50e-26	38.69	2.16e-25	57.60	1.06e-24	64.28
r61	CO + C2O	C + C2O2	462.97	k61 (G20; [k40, k61])	cm^3 $molecules^{-1}$ s^{-1}	7.44e-25	14.05	1.68e-24	39.34	1.16e-24	33.24	1.12e-24	5.35
r62	C + C2O2	CO + C2O	-462.97	k62 (G2; [k88, k62, k42])	cm^3 $molecules^{-1}$ s^{-1}	2.75e-25	51.87	3.06e-25	32.14	2.23e-25	8.76	1.77e-24	36.66
r63	CO + O2	C + O3	969.58	k63 (G23; [k12, k65, k63])	cm^3 $molecules^{-1}$ s^{-1}	7.17e-26	15.67	1.35e-26	3.74	8.54e-26	13.74	1.45e-26	3.01
r64	C + O3	CO + O2	-969.58	k64 (G6; [k14, k64])	cm^3 $molecules^{-1}$ s^{-1}	2.81e-24	5.94	7.12e-24	48.14	1.31e-23	64.12	1.29e-25	1.19
r65	CO + O2	CO3	-13.13	k65 (G23; [k12, k65, k63])	cm^3 $molecules^{-1}$ s^{-1}	4.08e-26	8.92	3.94e-26	10.92	2.17e-25	34.92	2.13e-25	44.15
r66	CO3 + RAD	CO + O2	13.13	k66 (G27; [k16, k66])	s^{-1}	4.53e-03	1.04	4.48e-03	1.8	2.01e-03	0.55	2.60e-02	25.79
r67	CO + O3	O + CO3	89.32	k67 (G24; [k18, k67])	cm^3 $molecules^{-1}$ s^{-1}	8.26e-26	29.13	2.35e-26	24.35	4.53e-26	37.72	2.38e-26	23.47
r68	O + CO3	CO + O3	-89.32	k68 (G32; [k20, k68])	cm^3 $molecules^{-1}$ s^{-1}	1.40e-26	40.82	2.42e-27	16.22	4.85e-26	21.04	1.91e-27	2.73
r69	O2 + RAD	O + O	493.68	k69 (single)	s^{-1}	4.95e-02	100	8.08e-01	100	1.95e-01	100	4.85e-01	100
r70	O + O	O2	-493.68	k70 (single)	cm^3 $molecules^{-1}$ s^{-1}	≤5.7e-31	100	≤5.9e-31	100	≤5.9e-31	100	1.23e-26	100
r71	O3 + RAD	O + O2	102.45	k71 (single)	s^{-1}	2.30e-03	100	6.54e-03	100	1.19e-02	100	1.21e-02	100
r72	O + O2	O3	-102.45	k72 (single)	cm^3 $molecules^{-1}$ s^{-1}	3.42e-26	100	4.93e-27	100	5.18e-26	100	2.65e-25	100
r73	C2 + RAD	C + C	602.45	k73 (single)	s^{-1}	8.21e-04	100	2.31e-02	100	9.81e-03	100	1.84e-02	100
r74	C + C	C2	-602.45	k74 (single)	cm^3 $molecules^{-1}$ s^{-1}	≤5.7e-31	100	≤5.9e-31	100	9.72e-26	100	1.80e-26	100
r75	C2O3 + RAD	O + C2O2	543.94	k75 (G13; [k28, k75, k77, k99, k101])	s^{-1}	2.45e-01	16.30	7.54e-01	46.09	2.12e-01	21.36	3.83e-01	41.95
r76	O + C2O2	C2O3	-543.94	k76 (G29; [k30, k76])	cm^3 $molecules^{-1}$ s^{-1}	1.44e-24	47.52	8.08e-25	10.68	3.38e-25	10.34	1.23e-25	2.03
r77	C2O3 + RAD	O2 + C2O	659.32	k77 (G13; [k28, k75, k77, k99, k101])	s^{-1}	4.16e-01	27.68	2.46e-01	15.04	7.73e-03	0.78	3.24e-02	3.55
r78	O2 + C2O	C2O3	-659.32	k78 (G33; [k32, k78])	cm^3 $molecules^{-1}$ s^{-1}	3.74e-24	17.61	4.22e-23	46.17	3.29e-24	10.38	3.06e-24	28.62
r79	C3 + RAD	C + C2	717.07	k79 (single)	s^{-1}	3.68e-02	100	3.27e-02	100	2.21e-02	100	1.69e-02	100
r80	C + C2	C3	-717.07	k80 (single)	cm^3 $molecules^{-1}$ s^{-1}	3.05e-27	100	≤5.9e-31	100	5.85e-26	100	≤5.7e-31	100
r81	C3O + RAD	C + C2O	758.51	k81 (G14; [k83, k85, k81])	s^{-1}	6.93e-04	0.09	9.23e-04	0.34	2.08e-04	0.50	1.09e-03	13.75
r82	C + C2O	C3O	-758.51	k82 (G1; [k82, k60])	cm^3 $molecules^{-1}$ s^{-1}	2.91e-26	16.81	7.13e-26	61.31	1.59e-25	42.40	5.89e-25	35.72
r83	C3O + RAD	C2 + CO	376.53	k83 (G14; [k83, k85, k81])	s^{-1}	6.35e-01	86.84	2.33e-01	84.97	3.12e-02	75.51	6.35e-03	80.09
r84	C2 + CO	C3O	-376.53	k84 (G7; [k84, k59])	cm^3 $molecules^{-1}$ s^{-1}	1.11e-24	100	1.56e-25	82.11	2.93e-24	98.97	3.17e-24	93.79
r85	C3O + RAD	O + C3	731.49	k85 (G14; [k83, k85, k81])	s^{-1}	9.55e-02	13.06	4.03e-02	14.7	9.91e-03	23.98	4.89e-04	6.17
r86	O + C3	C3O	-731.49	k86 (single)	cm^3 $molecules^{-1}$ s^{-1}	8.48e-25	100	2.32e-24	100	9.29e-24	100	7.36e-25	100

Table 3 – *continued*

Reaction label	Reactions parameters					10 K (this wok)		13 K irradiated by 50 MeV Ni ions (Pilling et al. 2023a)		15 K (this wok)		20 K (this wok)	
	Reactants	Products	$\Delta_r H$	k label**	k unit	k value	BR (per cent)	k value	BR(per cent)	k value	BR (per cent)	k value	BR (per cent)
r87	C3O2 + RAD	C + C2O2	828.3	k87 (G15; [k89, k91, k87, k93])	s^{-1}	1.25e-01	35.55	4.48e-01	27.65	2.69e-01	32.70	7.73e-02	16.16
r88	C + C2O2	C3O2	-828.3	k88 (G2; [k88, k62, k42])	cm^3 $molecules^{-1}$ s^{-1}	2.21e-25	41.68	5.26e-25	55.25	2.24e-24	87.97	2.86e-24	59.24
r89	C3O2 + RAD	C2 + CO2	529.23	k89 (G15; [k89, k91, k87, k93])	s^{-1}	1.33e-01	37.82	7.64e-01	47.16	3.33e-01	40.48	2.12e-01	44.32
r90	C2 + CO2	C3O2	-529.23	k90 (G8; [k90, k39, k41])	cm^3 $molecules^{-1}$ s^{-1}	4.78e-23	80.84	4.72e-24	66.37	2.33e-24	50.72	1.15e-24	17.94
r91	C3O2 + RAD	O + C3O	678.85	k91 (G15; [k89, k91, k87, k93])	s^{-1}	9.30e-02	26.45	4.08e-01	25.18	2.20e-01	26.74	1.87e-01	39.10
r92	O + C3O	C3O2	-678.85	k92 (single)	cm^3 $molecules^{-1}$ s^{-1}	1.04e-23	100	7.13e-24	100	3.14e-23	100	3.34e-23	100
r93	C3O2 + RAD	O2 + C3	916.66	k93 (G15; [k89, k91, k87, k93])	s^{-1}	6.48e-04	0.18	1.17e-04	0.01	6.88e-04	0.08	2.02e-03	0.42
r94	O2 + C3	C3O2	-916.66	k94 (single)	cm^3 $molecules^{-1}$ s^{-1}	1.86e-25	100	1.66e-25	100	6.37e-26	100	1.98e-26	100
r95	C2O2 + RAD	O + C2O	609.06	k95 (G12; [k48, k26, k95, k97])	s^{-1}	3.91e-03	0.45	1.05e-02	1.0	3.82e-03	0.98	1.80e-03	0.42
r96	O + C2O	C2O2	-609.06	k96 (G28; [k52, k96])	cm^3 $molecules^{-1}$ s^{-1}	3.65e-23	50.55	2.93e-23	38.4	1.14e-23	20.73	9.22e-25	4.70
r97	C2O2 + RAD	C2 + O2	805.43	k97 (G12; [k48, k26, k95, k97])	s^{-1}	2.46e-03	0.28	8.59e-04	0.08	5.78e-04	0.15	1.30e-04	0.03
r98	C2 + O2	C2O2	-805.43	k98 (G9; [k50, k98, k22])	cm^3 $molecules^{-1}$ s^{-1}	4.13e-23	60.59	1.57e-23	29.97	1.12e-24	2.89	3.37e-24	11.27
r99	C2O3 + RAD	C + CO3	866.66	k99 (G13; [k28, k75, k77, k99, k101])	s^{-1}	9.58e-03	0.64	3.93e-02	2.4	2.08e-02	2.10	8.50e-03	0.93
r100	C + CO3	C2O3	-866.66	k100 (single)	cm^3 $molecules^{-1}$ s^{-1}	1.17e-26	100	1.13e-26	100	8.01e-26	100	4.89e-25	100
r101	C2O3 + RAD	C2 + O3	1246.92	k101 (G13; [k28, k75, k77, k99, k101])	s^{-1}	1.53e-03	0.10	6.02e-04	0.04	1.18e-03	0.12	1.26e-04	0.01
r102	C2 + O3	C2O3	-1246.92	k102 (G10; [k34, k102])	cm^3 $molecules^{-1}$ s^{-1}	2.54e-24	16.24	5.42e-24	11.55	2.46e-24	30.67	5.25e-24	9.90
r103	C4O + RAD	C + C3O	468.37	k103 (G16; [k107, k103, k105])	s^{-1}	8.75e-02	59.13	1.26e-01	19.47	6.79e-02	11.11	7.55e-02	36.60
r104	C + C3O	C4O	-468.37	k104 (single)	cm^3 $molecules^{-1}$ s^{-1}	9.41e-26	100	1.72e-25	100	1.45e-25	100	6.26e-26	100
r105	C4O + RAD	C2 + C2O	624.43	k105 (G16; [k107, k103, k105])	s^{-1}	3.19e-03	2.16	1.82e-02	2.81	7.45e-03	1.22	1.88e-02	9.11
r106	C2 + C2O	C4O	-624.43	k106 (single)	cm^3 $molecules^{-1}$ s^{-1}	2.49e-26	100	2.56e-26	100	3.59e-26	100	4.06e-26	100
r107	C4O + RAD	CO + C3	127.83	k107 (G16; [k107, k103, k105])	s^{-1}	5.73e-02	38.72	5.03e-01	77.72	5.36e-01	87.67	1.12e-01	54.29
r108	CO + C3	C4O	-127.83	k108 (single)	cm^3 $molecules^{-1}$ s^{-1}	1.48e-25	100	1.53e-25	100	3.70e-26	100	2.92e-26	100
r109	C4O2 + RAD	C + C3O2	455.59	k109 (G17; [k115, k113, k109, k117, k111])	s^{-1}	1.01e-01	17.85	1.22e-01	11.45	5.63e-02	6.97	5.64e-01	24.26
r110	C + C3O2	C4O2	-455.59	k110 (single)	cm^3 $molecules^{-1}$ s^{-1}	1.22e-25	100	1.09e-26	100	5.89e-26	100	3.91e-26	100
r111	C4O2 + RAD	C2 + C2O2	681.44	k111 (G17; [k115, k113, k109, k117, k111])	s^{-1}	8.31e-04	0.15	1.02e-03	0.1	7.16e-03	0.89	1.38e-02	0.59
r112	C2 + C2O2	C4O2	-681.44	k112 (single)	cm^3 $molecules^{-1}$ s^{-1}	4.93e-26	100	4.78e-26	100	7.26e-26	100	1.12e-26	100
r113	C4O2 + RAD	C3 + CO2	267.75	k113 (G17; [k115, k113, k109, k117, k111])	s^{-1}	1.14e-01	20.15	5.10e-01	47.86	3.91e-01	48.42	7.47e-01	32.13
r114	C3 + CO2	C4O2	-267.75	k114 (single)	cm^3 $molecules^{-1}$ s^{-1}	6.83e-25	100	4.70e-25	100	1.15e-25	100	2.08e-25	100
r115	C4O2 + RAD	CO + C3O	62.41	k115 (G17; [k115, k113, k109, k117, k111])	s^{-1}	3.45e-01	60.99	3.92e-01	36.79	3.16e-01	39.13	5.39e-01	23.18
r116	CO + C3O	C4O2	-62.41	k116 (single)	cm^3 $molecules^{-1}$ s^{-1}	8.62e-26	100	1.26e-25	100	9.69e-26	100	7.18e-28	100
r117	C4O2 + RAD	O + C4O	666.07	k117 (G17; [k115, k113, k109, k117, k111])	s^{-1}	4.85e-03	0.86	4.05e-02	3.8	3.71e-02	4.59	4.61e-01	19.83
r118	O + C4O	C4O2	-666.07	k118 (single)	cm^3 $molecules^{-1}$ s^{-1}	1.12e-26	100	9.54e-27	100	3.85e-26	100	6.29e-26	100
r119	C5O + RAD	C + C4O	696.89	k119 (G18; [k121, k123, k119])	s^{-1}	1.93e-04	1.41	1.43e-03	2.77	2.34e-03	2.41	3.82e-03	0.45
r120	C + C4O	C5O	-696.89	k120 (single)	cm^3 $molecules^{-1}$ s^{-1}	8.81e-25	100	9.01e-25	100	1.48e-24	100	8.48e-25	100
r121	C5O + RAD	C2 + C3O	562.81	k121 (G18; [k121, k123, k119])	s^{-1}	1.29e-02	94.29	2.02e-02	39.12	9.04e-02	93.12	8.34e-01	97.34
r122	C2 + C3O	C5O	-562.81	k122 (single)	cm^3 $molecules^{-1}$ s^{-1}	1.20e-23	100	1.01e-23	100	1.45e-23	100	1.42e-24	100
r123	C5O + R	C3 + C2O	604.25	k123 (G18; [k121, k123, k119])	s^{-1}	5.88e-04	4.30	3.00e-02	58.11	4.34e-03	4.47	1.90e-02	2.22
r124	C3 + C2O	C5O	-604.25	k124 (single)	cm^3 $molecules^{-1}$ s^{-1}	4.63e-25	100	3.66e-24	100	2.58e-24	100	3.15e-25	100

Table 3 – *continued*

Reaction label	Reactions parameters					10 K (this wok)		13 K irradiated by 50 MeV Ni ions (Pilling et al. 2023a)		15 K (this wok)		20 K (this wok)	
	Reactants	Products	$\Delta_r H$	k label**	k unit	k value	BR (per cent)	k value	BR(per cent)	k value	BR (per cent)	k value	BR (per cent)
r125	C5O2 + RAD	C + C4O2	713.14	k125 (G19; [k133, k135, k129, k131, k127, k125])	s^{-1}	7.74e-04	0.03	1.52e-04	0.01	5.08e-04	0.02	1.74e-03	0.07
r126	C + C4O2	C5O2	-713.14	k126 (single)	cm^3 $molecules^{-1}$ s^{-1}	1.54e-26	100	3.87e-26	100	1.20e-25	100	1.62e-26	100
r127	C5O2 + RAD	O + C5O	682.32	k127 (G19; [k133, k135, k129, k131, k127, k125])	s^{-1}	2.03e-01	8.77	4.33e-01	14.53	5.45e-01	17.16	5.00e-02	1.95
r128	O + C5O	C5O2	-682.32	k128 (single)	cm^3 $molecules^{-1}$ s^{-1}	7.57e-27	100	1.85e-26	100	1.14e-25	100	3.81e-25	100
r129	C5O2 + RAD	C2 + C3O2	566.28	k129 (G19; [k133, k135, k129, k131, k127, k125])	s^{-1}	8.12e-01	35.06	4.46e-01	14.97	8.37e-01	26.36	7.09e-01	27.71
r130	C2 + C3O2	C5O2	-566.28	k130 (single)	cm^3 $molecules^{-1}$ s^{-1}	8.73e-26	100	1.66e-26	100	2.30e-25	100	1.39e-26	100
r131	C5O2 + RAD	C3 + C2O2	677.51	k131 (G19; [k133, k135, k129, k131, k127, k125])	s^{-1}	7.00e-01	30.23	5.52e-01	18.53	5.47e-01	17.23	4.37e-01	17.08
r132	C3 + C2O2	C5O2	-677.51	k132 (single)	cm^3 $molecules^{-1}$ s^{-1}	1.08e-25	100	5.21e-26	100	3.01e-25	100	4.84e-26	100
r133	C5O2 + RAD	CO + C4O	307.18	k133 (G19; [k133, k135, k129, k131, k127, k125])	s^{-1}	3.33e-01	14.38	7.12e-01	23.9	7.56e-01	23.81	7.09e-01	27.71
r134	CO + C4O	C5O2	-307.18	k134 (single)	cm^3 $molecules^{-1}$ s^{-1}	3.65e-24	100	6.33e-24	100	6.51e-24	100	2.40e-23	100
r135	C5O2 + RAD	C2O + C3O	555.08	k135 (G19; [k133, k135, k129, k131, k127, k125])	s^{-1}	2.67e-01	11.53	8.36e-01	28.06	4.90e-01	15.43	6.52e-01	25.48
r136	C2O + C3O	C5O2	-555.08	k136 (single)	cm^3 $molecules^{-1}$ s^{-1}	3.55e-26	100	5.53e-27	100	1.54e-25	100	1.70e-26	100
r137	O2 + O2	O + O3	391.23	k137 (single)	cm^3 $molecules^{-1}$ s^{-1}	8.52e-26	100	5.16e-27	100	3.60e-26	100	2.26e-27	100
r138	O + O3	O2 + O2	-391.23	k138 (single)	cm^3 $molecules^{-1}$ s^{-1}	3.94e-25	100	1.98e-25	100	1.41e-25	100	1.77e-25	100
r139	C desorption	–	NA	k139 (desorption)	s^{-1}	8.08e-04	100	1.87e-03	100	4.07e-03	100	2.25e-03	100
r140	O desorption	–	NA	k140 (desorption)	s^{-1}	8.60e-05	100	7.81e-05	100	1.68e-04	100	6.48e-04	100
r141	C2 desorption	–	NA	k141 (desorption)	s^{-1}	4.28e-05	100	5.25e-05	100	4.94e-05	100	2.51e-05	100
r142	CO desorption	–	NA	k142 (desorption)	s^{-1}	1.34e-05	100	1.45e-05	100	7.68e-11	100	2.81e-10	100
r143	O2 desorption	–	NA	k143 (desorption)	s^{-1}	1.24e-04	100	4.97e-04	100	4.25e-04	100	2.06e-02	100
r144	C3 desorption	–	NA	k144 (desorption)	s^{-1}	8.88e-05	100	1.60e-04	100	8.15e-05	100	1.13e-02	100
r145	C2O desorption	–	NA	k145 (desorption)	s^{-1}	9.16e-04	100	2.87e-04	100	1.28e-04	100	3.43e-04	100
r146	CO2 desorption	–	NA	k146 (desorption)	s^{-1}	3.73e-04	100	7.29e-04	100	5.84e-04	100	7.36e-03	100
r147	O3 desorption	–	NA	k147 (desorption)	s^{-1}	1.92e-05	100	2.37e-05	100	2.41e-05	100	6.34e-04	100
r148	C3O desorption	–	NA	k148 (desorption)	s^{-1}	9.68e-04	100	5.60e-04	100	2.44e-03	100	1.59e-03	100
r149	C2O2 desorption	–	NA	k149 (desorption)	s^{-1}	4.42e-05	100	8.61e-04	100	4.70e-04	100	2.29e-02	100
r150	CO3 desorption	–	NA	k150 (desorption)	s^{-1}	8.19e-04	100	7.73e-04	100	4.04e-03	100	5.13e-03	100
r151	C4O desorption	–	NA	k151 (desorption)	s^{-1}	3.49e-04	100	8.49e-04	100	1.90e-03	100	2.36e-02	100
r152	C3O2 desorption	–	NA	k152 (desorption)	s^{-1}	1.12e-04	100	7.06e-05	100	9.92e-05	100	4.37e-04	100
r153	C2O3 desorption	–	NA	k153 (desorption)	s^{-1}	9.87e-05	100	1.92e-04	100	2.75e-04	100	5.98e-03	100
r154	C5O desorption	–	NA	k154 (desorption)	s^{-1}	3.08e-05	100	1.08e-05	100	1.28e-06	100	2.30e-05	100
r155	C4O2 desorption	–	NA	k155 (desorption)	s^{-1}	2.28e-04	100	9.65e-04	100	2.09e-03	100	1.36e-03	100
r156	C5O2 desorption	–	NA	k156 (desorption)	s^{-1}	1.02e-05	100	1.20e-05	100	1.89e-05	100	6.74e-05	100

*RAD = Radiation (CRs and mainly the net effect of secondary radiation-produced particles within the ice, as fast electrons and ionizing photons, that might interact with frozen molecules)
**single reaction: (single); reaction within groups: (Group label; [Group members ranked by thermochemistry only with the most exothermic first]); intrinsic desorption: (desorption)
NA: Not applied

Table 4. Average values for the ERCs and desorption obtained by the best-fitting model considered in the mapping of the chemical evolution of pure CO ice irradiated by cosmic rays. A comparison with the average values obtained for pure CO_2 ices obtained by using a similar methodology (Pilling et al. 2023a) was also listed for comparison purposes.

Average parameter	10 K (this work)	Pure CO ice at 13 K irradiated by 50 MeV Ni ions (Pilling et al. 2023a)	15 K (this work)	20 K (this work)
ERC for the intrinsic desorption reactions (k_{des})	2.8e-04 s^{-1}	4.4e-04 s^{-1}	9.3e-04 s^{-1}	5.8e-03 s^{-1}
ERC for direct dissociation reactions	1.6e-01 s^{-1}	2.4e-01 s^{-1}	1.8e-01 s^{-1}	1.9e-01 s^{-1}
ERC for the bimolecular collisions reactions	4.2e-24 cm^3 molecules^{-1} s^{-1}	4.4e-24 cm^3 molecules^{-1} s^{-1}	2.9e-24 cm^3 molecules^{-1} s^{-1}	4.1e-24 cm^3 molecules^{-1} s^{-1}
Desorption rate	5.1e+13 molecules s^{-1}	7.4e+13 molecules s^{-1}	8.1e+13 molecules s^{-1}	8.1e+13 molecules s^{-1}
Desorption yield (Y) *	1.8e+05 molecules ion^{-1}	1.3e+05 molecules ion^{-1}	2.9e+05 molecules ion^{-1}	2.9e+05 molecules ion^{-1}

*The estimated experimental desorption yield for analogous experiment is $\geq$ 0.7e + 05 molecules ion^{-1} (Seperuelo-Duarte et al. 2010).

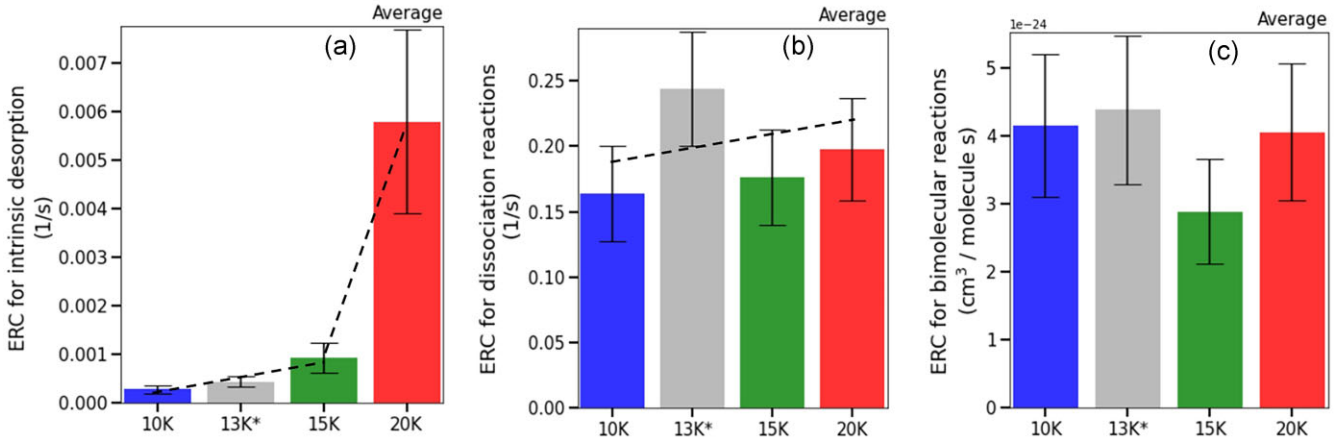

Figure 4. Average values for ERCs for radiation-induced intrinsic desorption (panel a), dissociation (panel b) and bimolecular reactions (panel c) for the different CO ice temperatures obtained in this work. ∗The value at 13 K was taken from Pilling et al. (2023a) and is from the best-fitting model of CO ice irradiated by 50 MeV Ni ions employing similar methodology. The dashed lines were inserted in the figures only to show the data tendency with the temperature. No clear tendency is observed in panel (c).

recently by Pilling et al. (2023c). The authors have analysed the chemical evolution and kinetics of water ice at four temperatures (12, 40, 60, and 90 K) employing the PROCODA code and have found that the average direct dissociation ERCs and bimolecular collision ERCs presented a decrease with the temperature in such ices. However, in the opposite way, the ERCs for the radiation-induced desorption and also the desorption rates (and yields) have increased with the temperature, corroborating the behaviour observed in this paper. Additionally, the authors observed that abundances at CE are sensitive to the ice´s temperature.

3.4 Thermochemistry behaviour of coupled ice-phase reactions (employing Van't Hoff equation methodology)

One interesting feature observed among the results was that some ERCs have decreased with temperature while others have increased. The next paragraphs focus on this issue and a discussion on the thermochemical behaviour of such solid-phase reactions. It is worth noting that such behaviour for ERCs was also noted before in the irradiation of water ices by energetic electrons (Pilling et al. 2023c).

In consideration of temperature dependence, it is imperative to acknowledge the presence of experimental uncertainties, the relatively constrained temperature range, and the minor divergences introduced by the best-fitting model. Nevertheless, we will illustrate that it remains feasible to derive overarching trends and averages that exhibit consistency across diverse analytical approaches in the majority of instances while dismissing outcomes with low correlations.

Fig. 5 highlights which reactions have ERCs for direct dissociation that increase or decrease with the temperature. Panel (a) presents the ERCs that follow the temperature enhancement and the opposite behaviour is presented in Panel (b). We observe that most reactions have ERCs values that increase with temperature (which are interpreted as having a positive activation energy), including for example CO_2 + RAD → O + CO (reaction r1), C_2O + RAD →C + CO (reaction r54), O_2 + RAD →O + O (reaction r69), and others (interpreted as an overall downhill process in the potential energy). However, some reactions present ERCs that decreases with temperature including CO_2 + RAD → C + O_2 (reaction r3) and others. In this methodology, we considered that few reactions were not sensitive enough (with variation less than 30 per cent) to temperature changes including the reactions CO + RAD → C + O (reaction r45), and reactions r26, r99, r103, and r129 (they were not listed in this figure).

The set of ERCs for bimolecular collisions that increase or decrease with the temperature is presented in Fig. 6. Panel (a) presents the ERCs that follow the temperature enhancement and the opposite behaviour is presented in panel (b). The non-indicated ERCs of bimolecular reactions in this figure were virtually non-sensible to the temperature changes. Mostly bimolecular reactions seem to have

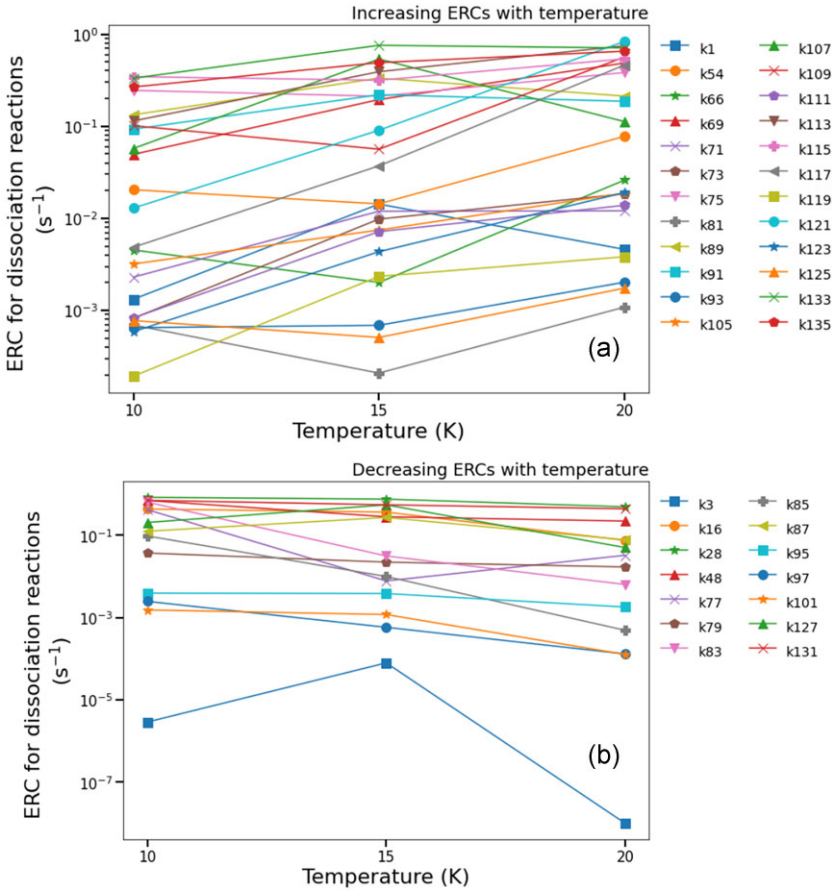

Figure 5. Influence of temperature in the ERCs for dissociation reactions. Panel (a) presents the ERCs that increases with temperature enhancement and the opposite behaviour is presented in panel (b). The reactions with variation of less than 30 per cent were considered not sensitive enough to temperature and are not listed in the figures.

ERC values that increase with the temperature, for example, O + CO → CO_2 (reaction r2) and CO + CO → C_2O_2 (reaction r47) and others. It is worth noting that reactions CO + CO_2→ C_2O_3 (reaction 27) and CO + CO_2 → C_2 + O_3 (reaction r33) have presented a very large increase in the ERCs with the temperature. This figure also shows that several reactions present decreasing ERCs with temperature, including for example CO_2 + CO_2 → O_2 + C_2O_2 (reaction r5), CO_2 + CO_2 → O + C_2O_3 (reaction r7), and others. The most dramatic decrease of ERCs with temperature was observed for the reactions CO + CO → C + CO_2 (reaction r24) and CO + CO → C_2 + O_2 (reaction r49).

It is known that the temperature affects the reaction rates by increasing the collisional frequency and increasing the average kinetic energy (allowing more collisions to overcome the activation energy). Furthermore, an enhanced complexity arises upon irradiation, where the nascent species may undergo a multitude of processes such as electronic excitation (which changes the activation energy itself) and the new species may have different desorption profiles at different temperatures (see also Steinfeld et al. 1998; Soustelle 2011; Atkins et al. 2018). Additionally, the specific reaction mechanisms and the involvement of intermediate species can also play a role in the temperature dependence of reaction rates. Complex reaction networks and competition between different pathways can lead to different temperature dependencies for different reactions. It's worth noting that the detailed understanding of these temperature-dependent trends requires a detailed analysis of the reaction mechanisms, energetics, and molecular dynamics involved in the irradiation of astrophysical ices.

It is worth noting that for radiation-induced dissociation reactions, the collisional frequency has a minimum importance since the reaction is triggered by the incoming radiation or its radiation products such as secondary electrons and secondary ionizing photons inside matter. Therefore in such reactions, the incoming flux plays an important role in the process as highlighted, for example, by Tarafdar (1992) and Heays et al. (2017). In the case of bimolecular collision reactions, as the temperature increases, the molecules move faster (in ices this is related to larger diffusion processes and/or enhancing in tunnelling effects), and therefore the frequency of collisions increases and thus k. In addition, the proportion of collisions that can overcome the activation energy for the reaction increases with temperature, and this allows an increase in the reaction rate coefficient. Such phenomenon is well described by the Arrhenius equation (e.g. Arrhenius 1889; Laidler 1984; Mills et al. 1993).

$$k = A\, e^{\frac{-E_a}{RT}}, \tag{4}$$

where k is the rate coefficient at a temperature T (in units of K), A is the pre-exponential factor (typically determined from experiments, and is a function of the frequency of collisions, the temperature and the type of reaction, and other factors), E_a is the activation energy for the reaction (in the same units as RT), $R = 8.314$ J K^{-1} mol^{-1} is the ideal gas constant.

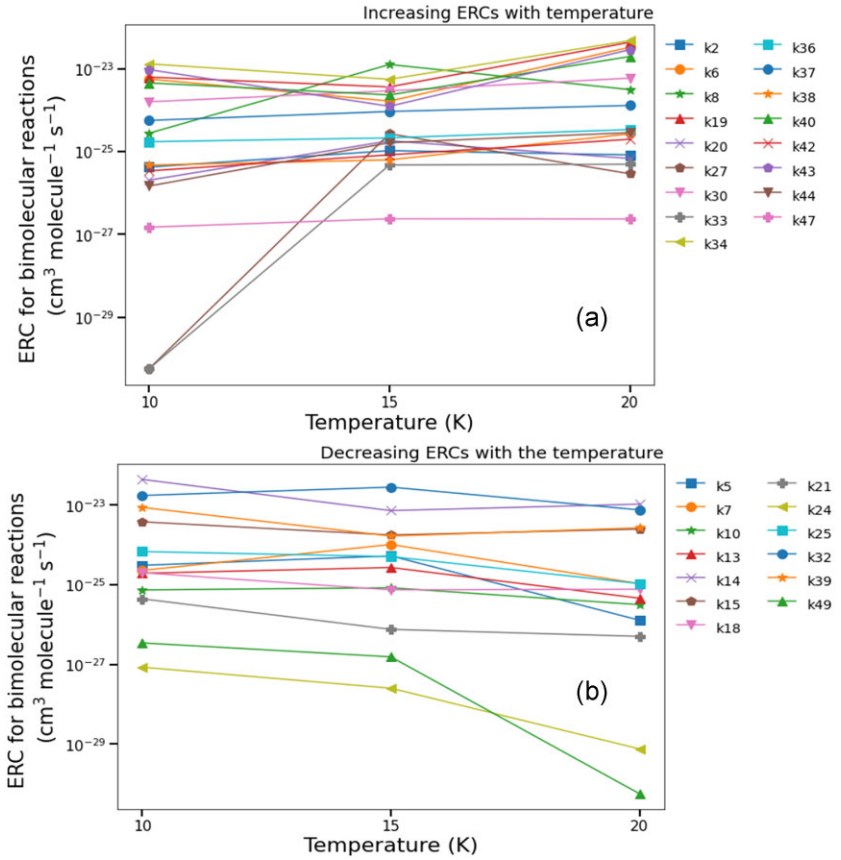

Figure 6. Influence of temperature in the ERCs of bimolecular reactions. Panel (a) presents the ERCs that follow the temperature enhancement and the opposite behaviour is presented in panel (b). The reactions with variation of less than 30 per cent were considered not sensitive enough to temperature and are not listed in the figures.

To suggest a thermochemistry behaviour of reactions in ice-phase (even understanding that they are coupled), we develop a methodology considering the values of ks (ERCs) at two temperatures and employing Van't Hoff equation as discussed below.

Considering the Van't Hoff equation (e.g. Van't Hoff 1884; Atkins et al. 2018) for reaction pair (e.g. $A + B \overset{k_{\mathrm{for},Ti}}{\rightarrow} C + D$ and $C + D \overset{k_{\mathrm{bck},Ti}}{\rightarrow} A + B$) in the chemical equilibrium phase

$$\ln\left(\frac{K_{T2}}{K_{T1}}\right) = \ln\left(\frac{k_{\mathrm{for},T2}/k_{\mathrm{bck},T2}}{k_{\mathrm{for},T1}/k_{\mathrm{bck},T1}}\right) = \frac{\Delta_r H^\circ}{R}\left(\frac{1}{T_1} - \frac{1}{T_2}\right), \qquad (5)$$

where $K_{Ti} = k_{\mathrm{for},Ti}/k_{\mathrm{bck},Ti}$ is the equilibrium constant and $k_{\mathrm{for},Ti}$ and $k_{\mathrm{bck},\,Ti}$ are the rate coefficients of the forward and reverse (backward) equations at a given temperature T_i, $\Delta_r H^\circ$ is the standard enthalpy of the forward reaction, and R is the ideal gas constant. An increase in the temperature changes the chemical equilibrium towards the endothermic branch of the reaction pair (thermodynamically more favourable when more energy is available in the system). In other words, for endothermic reactions ($\Delta_r H^\circ > 0$) when temperature increases ($T_2 > T_1$) we will have $(\frac{1}{T_1} - \frac{1}{T_2}) > 0$ and, consequently, $\ln(\frac{k_{\mathrm{for},\,T2}/k_{\mathrm{bck},T2}}{k_{\mathrm{for},T1}/k_{\mathrm{bck},T1}}) > 0$ indicating that $k_{\mathrm{for},T2}/k_{\mathrm{bck},T2} > k_{\mathrm{for},T1}/k_{\mathrm{bck},T1}$ or $k_{\mathrm{for},T2}/k_{\mathrm{for},T1} > k_{\mathrm{bck},T2}/k_{\mathrm{bck},T1}$. When the considered temperatures are, for example, $T_1 = 10$ K and $T_2 = 20$ K, such endothermic reactions present a positive slope in a graph showing $(k_{\mathrm{for},Ti}/k_{\mathrm{bck},\,Ti})/(k_{\mathrm{for},\,10K}/k_{\mathrm{bck},10K})$ versus the temperature. In other words, this would indicate that if there is an increase of k in the forward reaction with the temperature, there would be an even greater increase in the backward reaction, which in chemical equilibrium could favour the formation of products. In case of exothermic reactions ($\Delta_r H^\circ < 0$), the same type of graph will show negative slopes. Similarly, this would indicate that if there is a decrease in k in the forward reaction with the temperature, there would be a smaller decrease in the backward reaction, which in chemical equilibrium could favour the formation of reactants. Both possibilities can be observed in Fig. 7 for the studied reactions pairs.

Fig. 7 presents the ratio between forward and reverse reaction rate coefficients at the temperatures of 10 K and 20 K normalized by the ratio at 10 K. As discussed before the analysis of this ratio suggests a thermochemistry behaviour (to be endothermic or exothermic) of some chemically coupled reactions in the irradiated frozen CO ice. A positive slope indicates endothermic reactions and a negative slope indicates exothermic reactions. Here, we did not consider reactions with values within the region named 'small change regions ($< \pm 50$)' due to eventual methodology uncertainty. In this figure, the caption labels indicate the selected reaction pair (forward/reverse reaction) and its thermochemistry behaviour (ENDO or EXO for endothermic or exothermic, respectively).

Note that, typically, endothermic reactions always have positive activation energy, and its ERC should increase with temperature. We highlight that most reactions deemed as ENDO by the Van't Hoff analysis also have a positive ERC dependence with temperature (see also Figs 5 and 6), and thus both analyses showed consistency. The exception here is $C_3 + RAD \rightarrow C + C_2$ (r79), which presents only modest temperature dependence to begin with.

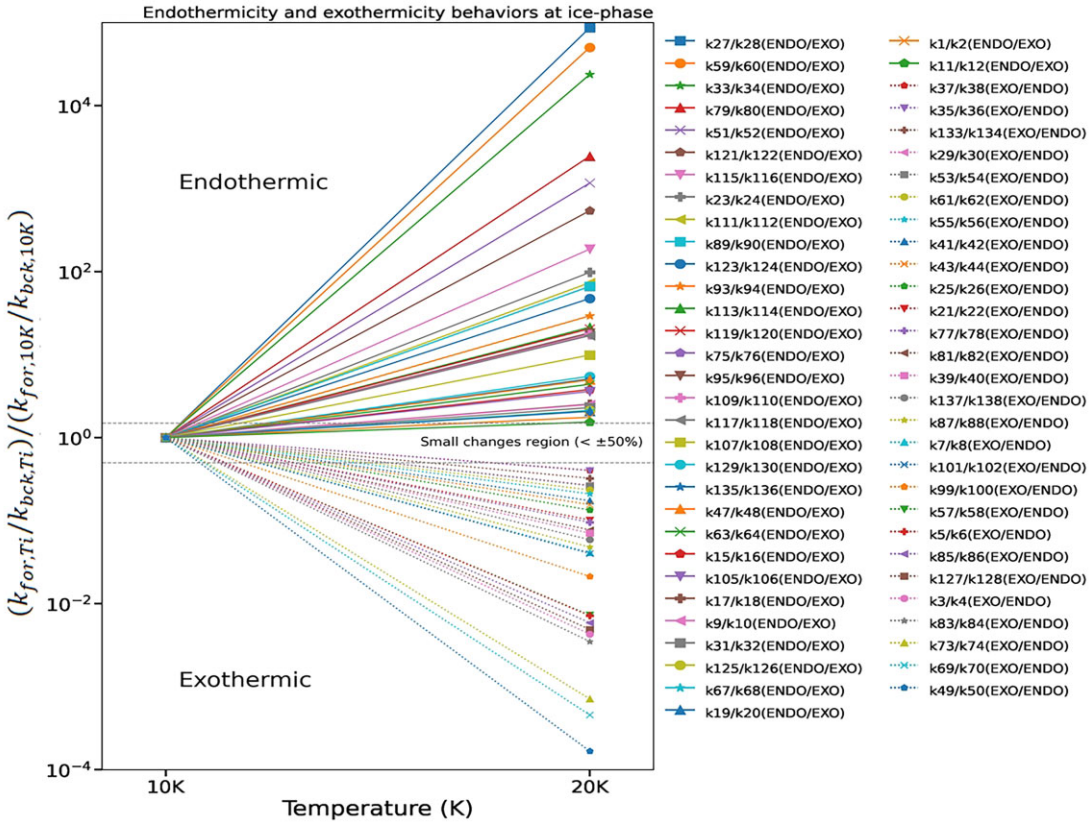

Figure 7. Ratio between forward and reverse (or backward) reaction rate coefficients at the temperatures of 10 K and 20 K normalized by the ratio at 10 K, suggesting a thermochemistry behaviour (to be endothermic or exothermic) of some chemically coupled reactions in the irradiated frozen CO ice. Here, we not considered the reactions with values within the region named 'small change regions ($< \pm 50$)' due to the methodology uncertainty. Labels indicate the selected reaction pair (forward/reverse reaction) and their thermochemistry behaviour (ENDO or EXO for endothermic or exothermic, respectively). See details in the text and also the Table B1 in the Appendix B.

In Appendix B (see Table B1) we present the suggested thermochemistry behaviour (to be endothermic or exothermic) studied ice-phase reactions derived by employing Van´t Hoff equation methodology (see also Fig. 7). For comparison, the reaction enthalpy and its thermochemistry behaviour for the single reactions in the gas-phase (employed in phase 1 calculations of PROCODA) are listed.

By comparing isolated gas-phase reaction with ice-phase chemically coupled reaction under incoming energy delivered by ionizing radiation (e.g. ice irradiation by cosmic-ray analogues) we observe in Table 4 that most reactions (∼62 per cent) present a similar thermochemistry behaviour, being endothermic or exothermic, in both phases. Among this group are, for example, the endothermic/exothermic reaction pairs r1/r2, r9/10, r11/12, r15/16, r17/18, r19/r20, r27/r28, r31/r32, r33/r34, r47/r48, r51/r52, r59/r60, r63/r64, r67/r68, r75/r76, r79/r80, r89/r90, r93/r94, r95/r96, r97/r98, r105/r106, r107/r108, r109/r110, r111/r112, r113/r114, r115/r116, r117/r118, r119/r120, r121/r122, r123/r124, r129/r130, and r135/r136, and the exothermic/endothermic reaction pairs r25/r26, r35/r36, r39/r40, and r53/54.

However, some reactions have presented an opposite thermochemistry behaviour between gas- and ice-phases. Among this group, almost all cases changed from being endothermic/exothermic in the gas phase to exothermic/endothermic in the ice, for example, the reaction pairs: r3/r4, r5/r7, r7/58, r21/r22, r29/r30, r37/38, r43/r44, r49/r50, r55/r56, r57/r58, r61/r62, r69/r70, r73/r74, r77/r78, r81/r82, r83/r84, r85/r86, r99/r100, r101/r102, r127/r127, r133/r134, and r137/138. Only one studied reaction pair, r23/r24, has changed in the opposite way, from exothermic/endothermic in the gas-phase to endothermic/exothermic in the ice-phase. It is worth noting that for few reactions, due to small differences of $k_{\mathrm{for},\,Ti}/k_{\mathrm{bck},Ti}$ at the temperatures of 10 K and 20 K, we do not suggest any specific thermochemistry behaviour and additional studies must be performed to elucidate this issue (see also Table 4).

The changes in the thermochemical behaviour observed for some reactions comparing both gas- and ice-phase are probably related to the presence of the surrounding molecules. For example, in the case of ice-phase reactions, the presence of neighbour species close to the reactants and the chemically coupled system itself increases the complexity and the interdependence of the reaction parameters. In other words, the competition between different pathways and reactions in the mechanism can result in varied temperature dependencies and also changes in thermochemical behaviour in comparison with gas-phase (isolated reaction). Additionally, the presence of intermediates or the involvement of multiple steps in the dissociation process can lead to different temperature dependencies for different reactions. This becomes even more complex due to the presence of secondary radiation-induced particles such as fast electrons and ionizing photons within the ice.

Fig. 8 presents a drawing with the schematic energy diagram of the thermochemistry behaviours comparing reactions in gas- and ice-phases studied in this paper. Panels (a1) and (a2) present reactions with similar thermochemistry behaviour in both phases and

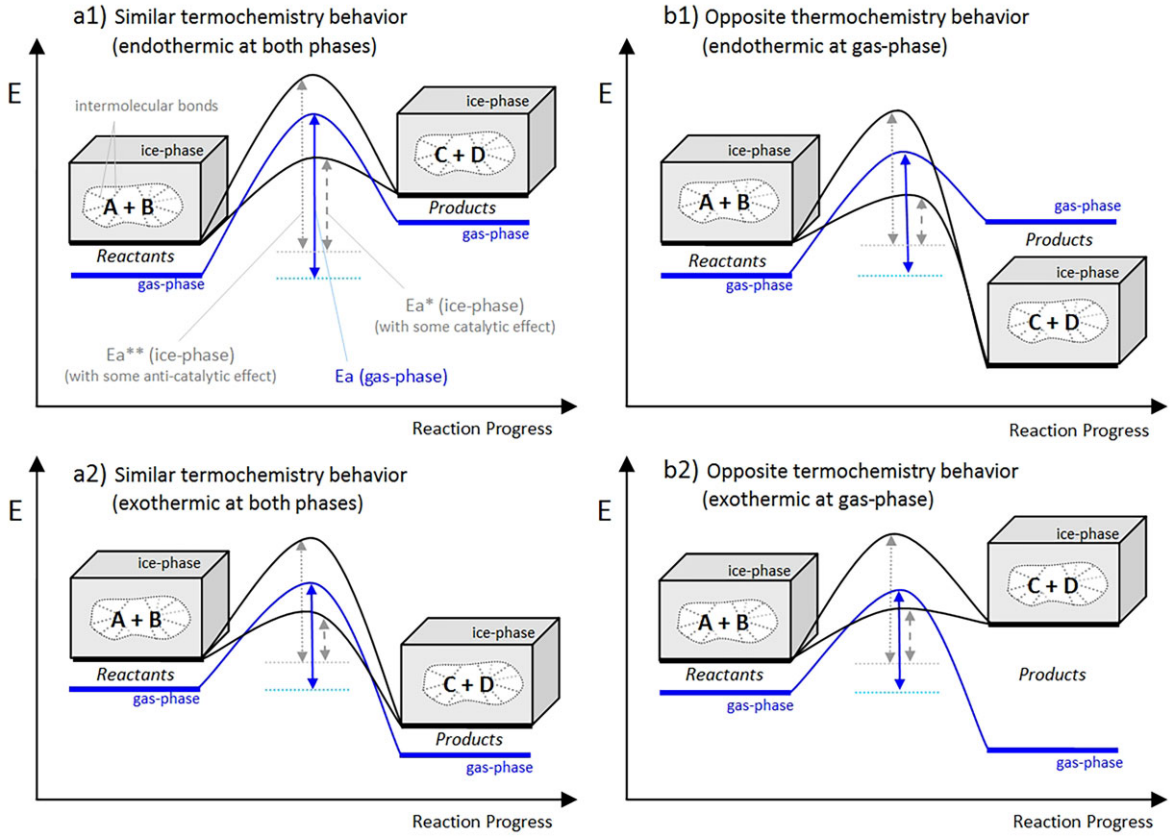

Figure 8. Schematic energy diagram of the thermochemistry behaviours comparing reactions in gas- and ice-phases studied in this paper. Panels (a1) and (a2) present a drawing of reactions with similar thermochemistry behaviour in both phases and panels (b1) and (b2) present a drawing of reactions with opposite thermochemistry behaviour between both phases. Lines in blue- and black-colour indicate gas- and ice-phase reactions progress, respectively. Ice-phase is also illustrated by a box containing the reactants (A + B) and products (C + D), having intermolecular bonds with the ice bulk (surrounding species). Vertical arrows indicate the eventual activating energy (Ea) of the reactions. For ice-phase two eventual activation energy was illustrated, one with a hypothetical catalytic effect (Ea∗) and the other with a hypothetical anti-catalytic affect (inhibitor) (Ea∗∗). Reactions with no activation barriers were omitted to avoid cartoon saturation. See details in the text.

panels (b1) and (b2) present reactions with opposite thermochemistry behaviour between both phases. Lines in blue- and black-colour indicate gas- and ice-phase reaction progress, respectively. Ice-phase is also illustrated by a box containing the reactants (A + B) and products (C + D) having intermolecular bonds with the ice bulk (surrounding species). As discussed by Alves et al. (2021), for example, during the study of the reaction $H_2O + CO \rightarrow HCOOH$ embedded in ice bulk, the presence of surrounding species may increase the activating barrier as well as slightly increase the energy of reactants and products due to interaction (intermolecular bonds) with the surrounding species. In this figure, the vertical arrows indicate the eventual activating energy (Ea) of the reactions. For the ice-phase, two possibilities for eventual activation energy were illustrated, one with a hypothetical catalytic effect (Ea∗) and the other with a hypothetical anticatalytic effect (inhibitor) (Ea∗∗). Reactions with no activation barriers were omitted to avoid saturation of the information presented in the figure.

Future experimental and theoretical investigations should focus on this issue in attempt to clarify the changes in the thermochemical behaviour observed for some ice-phase reactions in the presence of incoming radiation. It is known that the molecular geometry (also other molecular properties) of embedded species and reactions kinetics of embedded reactions are affected by the surrounding species in ices (e.g. Bonfim et al. 2017; Pilling & Bonfim 2020; Alves et al. 2021; Paiva et al. 2023). Future studies should go deeper on the effect of intermolecular bonds of embedded species with ice bulk (or surrounding species) to add new information on the thermochemistry and kinetics of embedded reactions in astrophysical ices.

3.5 Temperature influence on molecular abundances in the chemical equilibrium

Fig. 9 presents the molecular abundances at chemical equilibrium, written in terms of column density (in percentage), obtained by the best-fitting model in the studied ices. Panel (a) and (b) present the results in normal and log scale, respectively. Values at 13 K were obtained from the best-fitting model of CO ice irradiated by 50 MeV Ni ions employing a similar methodology (taken from Pilling et al. 2023a), presented for comparison purposes. This figure shows that the most produced species was atomic oxygen (>50 per cent) followed by atomic carbon (>15 per cent). The other important species at chemical equilibrium were CO (5–22 per cent), CO_2 (∼0.5–1 per cent), and CO_3 (∼0.05–0.1 per cent). From this figure, we also observe that the molecular abundance of most species, including, for example, CO, CO_2, C_2O, and CO_3, increases as function of the temperature. However, in the case of some species, for example, C, O, C_3, O_2, C_5O, and C_4O_2 we observed the opposite behaviour, decreasing molecular abundance as a function of the temperature. The numerical values of this figure are listed in Table 5

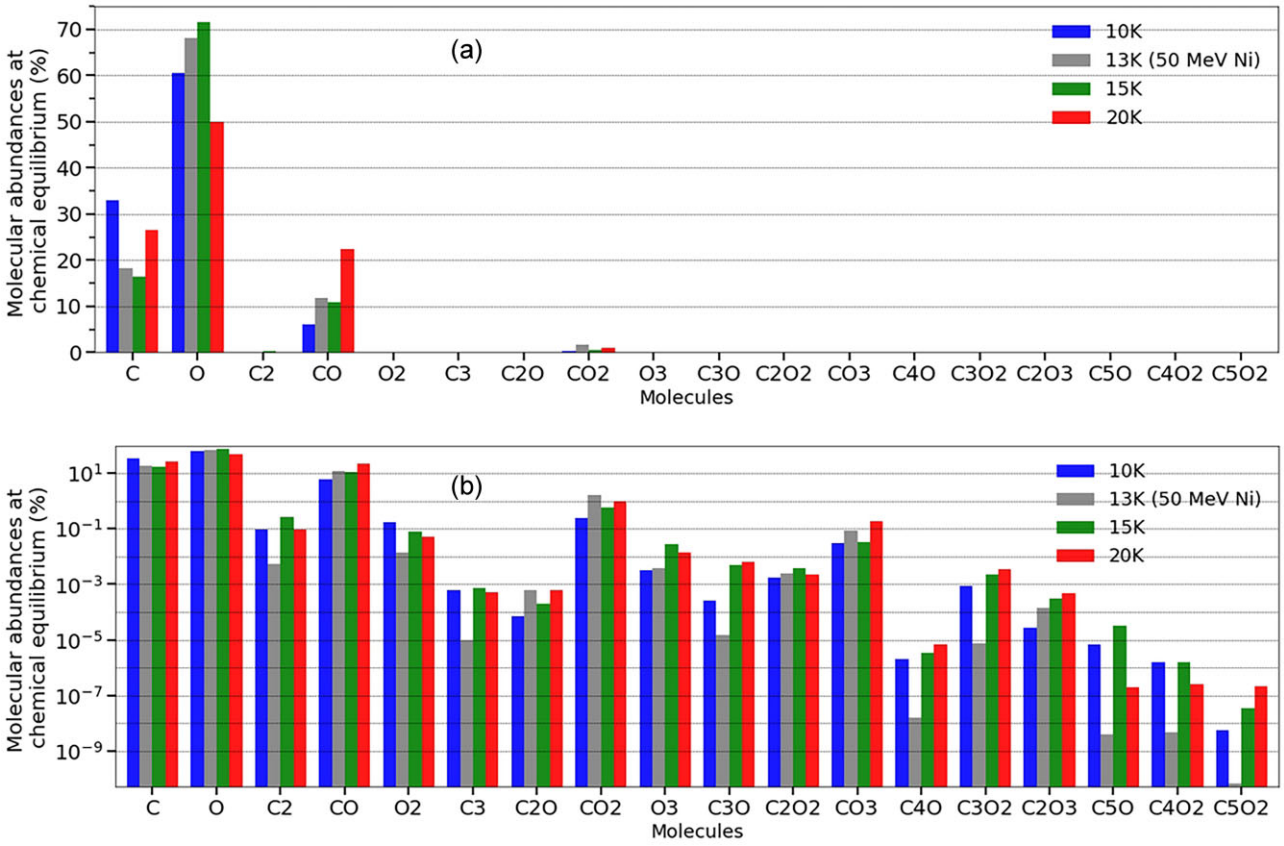

Figure 9. Molecular abundances at chemical equilibrium, in percentage. Panels (a) and (b) present the values in normal scale and log scale, respectively. The values at 13 K were obtained from the best-fitting model of CO ice irradiated by 50 MeV Ni ions employing a similar methodology (taken from Pilling et al. 2023a).

Table 5. List of the molecular abundances at the chemical equilibrium phase, in percentage, for the studied CO ices irradiated by 95.2 MeV Xe ions at different temperatures. For comparison, values from pure CO ice at 13 K irradiated by 50 MeV Ni ions (Pilling et al. 2023a) and from pure CO_2 ice at 13 K irradiated by 52 MeV Ni ions (Pilling et al. 2022a) employing PROCODA code were also listed.

Frozen species	Irradiated CO ice at 10 K (this work)	Irradiated CO ice at 13 K (Pilling et al. 2023a)	Irradiated CO ice at 15 K (this work)	Irradiated CO ice at 20 K (this work)	Irradiated CO_2 ice at 13 K (Pilling et al. 2022a)
C	32.8 per cent	18.2 per cent	16.4 per cent	26.4 per cent	23.1 per cent
O	60.6 per cent	68.1 per cent	71.7 per cent	49.8 per cent	30.4 per cent
C_2	0.09 per cent	0.05 per cent	0.3 per cent	0.09 per cent	0.8 per cent
CO	5.9 per cent	11.8 per cent	10.9 per cent	22.4 per cent	7.9 per cent
O_2	0.2 per cent	0.4 per cent	0.08 per cent	0.05 per cent	3.1 per cent
C_3	6e-4 per cent	1e-5 per cent	7e-4 per cent	5e-4 per cent	NQ
C_2O	6e-5 per cent	6e-4 per cent	1e-4 per cent	6e-4 per cent	0.1 per cent
CO_2	0.2 per cent	1.6 per cent	0.6 per cent	1.0 per cent	33.8 per cent
O_3	3e-3 per cent	4e-3 per cent	0.03 per cent	0.01 per cent	0.9 per cent
C_3O	2e-4 per cent	1e-5 per cent	5e-3 per cent	6e-3 per cent	NQ
C_2O_2	2e-3 per cent	2e-3 per cent	4e-3 per cent	2e-3 per cent	∼0 per cent
CO_3	0.03 per cent	0.09 per cent	0.03 per cent	0.2 per cent	<0.1 per cent
C_4O	2e-6 per cent	2e-8 per cent	3e-6 per cent	7e-6 per cent	NQ
C_3O_2	8e-4 per cent	7e-6 per cent	2e-3 per cent	3e-3 per cent	NQ
C_2O_3	3e-5 per cent	1e-4 per cent	3e-4 per cent	4e-4 per cent	∼0 per cent
C_5O	7e-6 per cent	4e-9 per cent	3e-5 per cent	2e-7 per cent	NQ
C_4O_2	2e-6 per cent	5e-9 per cent	2e-6 per cent	2e-7 per cent	NQ
C_5O_2	5e-9 per cent	7e-11 per cent	3e-8 per cent	2e-7 per cent	NQ

NQ – Not quantified.

in comparison with molecular abundances mapped previously in the irradiation of pure CO_2 ice by cosmic-ray analogues employing a similar methodology (see also Pilling et al. 2022a).

It is worth noting that in Fig. 9 we can also observe a peculiar behaviour happens at the temperature of 20 K. For example, we notice a strong production of C, CO, and CO_3, and a strong consumption of O. The larger species C_4O, C_5O_2, C_4O_2, and C_5O_2 have molecular abundances below 5e-5 per cent. Curiously, the species C_2O_2 and C_3O_2 present molecular abundances around 1e-3 per cent, larger than for C_2O. The numerical values of this figure are listed in Table 5.

Table 5 lists the molecular abundances at the chemical equilibrium phase, in percentage, for the studied CO ices irradiated by 95.2 MeV Xe ions at different temperatures. For comparison, values from pure CO ice at 13 K irradiated by 50 MeV Ni ions (Pilling et al. 2023a) and from pure CO_2 ice at 13 K irradiated by 52 MeV Ni ions (Pilling et al. 2022a) also employing PROCODA code were also listed.

Changes in the molecular abundances of crystalline water ices under processing by radiation as a function of temperature were also quantified and discussed by Pilling et al. (2023c) employing a similar computational methodology.

3.6 Temperature influence on radiation-induced desorption to gas phase

The influence of temperature on molecular radiation-induced desorption, evaluated at the chemical equilibrium phase, is shown in Fig. 10. In this figure, panel (a) presents the molecular desorption in percentage and panel (b) presents the desorption yield in units of molecules ion^{-1}. The values at 13 K were obtained from best-fitting model of CO ice irradiated by 50 MeV Ni ions employing a similar methodology (taken from Pilling et al. 2023a). The atomic carbon and oxygen represent the most desorbed species. For some species the increase in the ice temperature yield and increase in radiation-induced molecular desorption, as observed by the species O, CO_2, O_3, C_3O, C_2O_2, CO_3, and C_2O_3. However, other chemical species presented an opposite behaviour, decreasing the molecular radiation-induced desorption as temperature increases, for example, C, C_2, CO, C_3, C_2O, C_4O, C_5O, C_4O_2, and C_5O_2. Curiously, the radiation-induced desorption percentage of CO at a temperature below 13 K is higher than the desorption of CO_2 at the same temperature, but this has an opposite behaviour for the temperatures in the range of 15–20 K.

Another interesting finding here is that the radiation-induced desorption of CO decreases with the temperature, in the studied temperature range from 10 to 20 K, having a maximum value at 10 K. Considering that thermal desorption of non-irradiated pure CO starts at $\sim$ 21 K (Collings et al. 2004), this might suggest that during ice bombardment, the intermolecular coupling between this species and ice bulk decreases with ice temperature or an enhanced diffusion of CO occurs at a lower temperature in bombarded ices. This issue and other issues about radiation-induced desorption dependence with temperature should be deeply investigated in future publications.

The desorption yield at the chemical equilibrium phase, in terms of molecules ion^{-1}, presented in panel (b), follows the behaviour of molecular radiation-induced desorption presented in panel (a). The atomic species presented a desorption yield larger than 10^4 particles ion^{-1} and the less desorbed species (the large molecular and less abundant species) presented a desorption yield of about 10^{-4} molecules ion^{-1}.

The average values for the ERCs of radiation-induced desorption reactions calculated by the model at different ice temperatures are presented at Fig. 11. We observe that ice's temperature affects directly the overall radiation-induced desorption indicating that more molecules are ejected into gas-phase during ice bombardment by cosmic rays at higher ice temperatures. It is worth noting that the desorption temperature of volatile species such as O_2, CO, and CO_2 in the non-irradiated pure ices are around 21 K, 21 K, and 79 K, respectively (Collings et al. 2004). This indicates that the current model suggests that even at lower temperatures such volatile species can be driven to gas phase by the incoming radiation.

A similar behaviour for radiation-induced desorption with increasing temperature was also observed during the analyses of the chemical evolution of crystalline water ices under processing by radiation employing PROCODA code [see also fig. 7 of Pilling et al. (2023c)] reinforcing that temperature favors desorption yields in irradiated astrophysical ices.

4. ASTROPHYSICAL IMPLICATIONS

The investigation into reaction kinetics and molecular abundances within astrophysical ices assumes paramount significance for unraveling the inherent chemical evolution within cold interstellar and planetary environments. The ISM's intricate chemical evolution hinges on numerous reactions, necessitating insight into their rate constants. With CO's ubiquity in astrophysical ices (e.g. Öberg et al. 2011; Boogert et al. 2015; Huang et al. 2020), understanding CO-rich ice reactions and kinetics is vital for unraveling universal organic chemistry evolution.

The considered ionizing source in this study is representative for the incoming energy of cosmic rays in astrophysical ices, mainly considering the ions within the iron group [see also Pilling et al. (2021, 2022b) and references therein]. As discussed in Appendix A, the effects of the employed Xe ion was similar to the effects of 50 MeV Ni ions [from exp. of Seperuelo-Duarte et al. (2010) and considered in previous manuscript of Pilling et al. (2023a) also employing the PROCODA code to map chemical evolution of cold CO ice]. However, in terms of chemistry production and radiation-induced desorption, we expect slight larger effects for Xe ions than for Ni or Fe ions.

The impact of ion bombardment on ices can be approximated, to some extent, through the use of X-rays or energetic electrons under certain conditions. However, it's important to emphasize that collisions involving energetic ions with matter characteristically result in significantly higher desorption rates and yields. This distinction creates a unique physicochemical landscape for these interactions, underscoring the critical relevance of investigations such as this study. Such research is imperative as it provides profound insights into the distinct mechanisms and outcomes engendered by energetic ion collisions, thereby enriching our understanding of astrochemical processes and the transformation of matter in space environments.

This current research, combining experimental and computational methods, bears four principal astrophysical implications: (i) characterizing and quantifying non-observed species within irradiated astrophysical ice analogues; (ii) quantifying molecular abundances (both observed and non-observed species) within irradiated ices at the chemical equilibrium phase; (iii) determining effective reaction rates coefficients (ERCs) for utilization in astrochemical models, aiding the comprehension of chemical evolution in cold ionized radiation-affected space environments; (iv) characterizing and quantifying radiation-induced desorption of frozen species into the gas phase.

Regarding the quantification of non-observed species within the ice matrix and the delineation of the chemical equilibrium phase, the present methodology serves a dual purpose: it aids in comprehending laboratory experiments involving the irradiation of cold astrophysical ice analogues (e.g. Pilling et al. 2009, 2010a, b, 2011a, b, 2012,

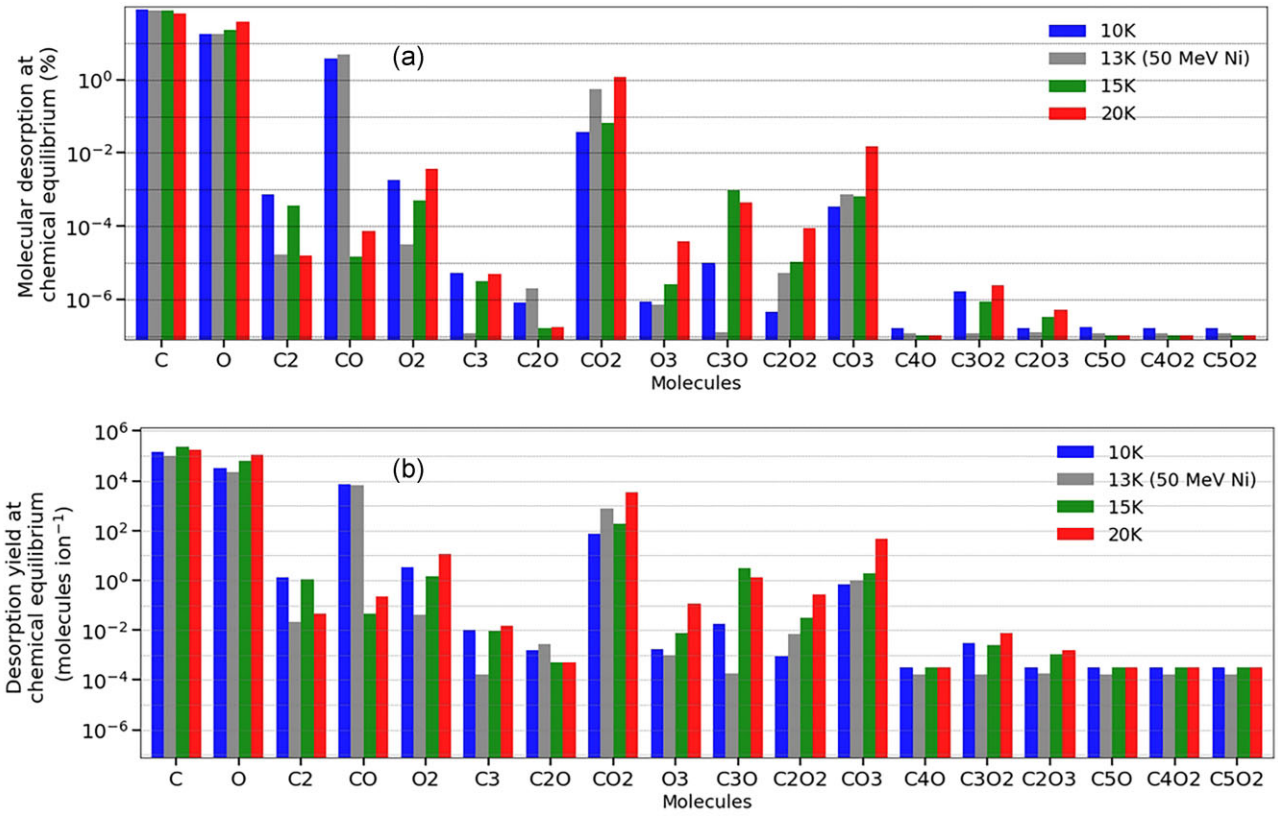

Figure 10. Molecular desorption at chemical equilibrium. Panel (a) presents the molecular desorption in percentage, and panel (b) presents the desorption yield in units of molecules ion^{-1}. The values at 13 K were obtained from the best-fitting model of CO ice irradiated by 50 MeV Ni ions employing a similar methodology (taken from Pilling et al. 2023a).

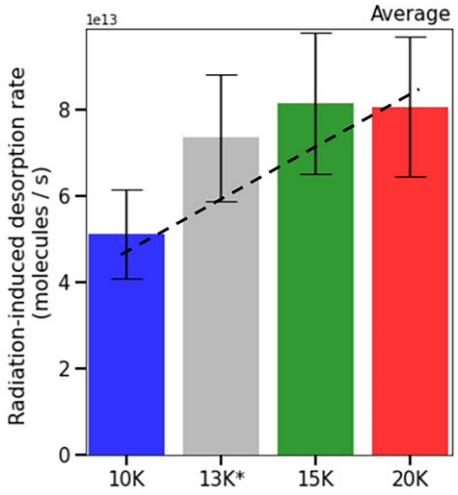

Figure 11. Average values for the ERCs of radiation-induced desorption reactions calculated by the model at different ice temperatures. The values at 13 K were obtained from the best-fitting model of CO ice irradiated by 50 MeV Ni ions employing a similar methodology (taken from Pilling et al. 2023a). The dashed line highlights the data tendency with the temperature.

2013; Domaracka et al. 2010; Boduch et al. 2011; Lv et al. 2012; Andrade et al. 2013; De Barros et al. 2014; Portugal et al. 2014, Bergantini et al. 2014a, b; Pilling and Bergantingi 2015; Almeida et al. 2017; Vasconcelos et al. 2017a, b, c; Bonfim et al. 2017; Freitas and Pilling 2020; Rachid et al. 2020; Vasconcelos et al. 2020), and it offers insights into astronomical observations of astrophysical ices facilitated by cutting-edge instruments like the *JWST* (e.g. Berné et al. 2023; McClure et al. 2023; Spilker et al. 2023).

On the determination of effective rate constants, this work provides essential data to be employed in astrochemical models. The astrochemical models conventionally encompass a range of pertinent physical and chemical mechanisms operative within the interstellar medium (ISM), including gas-phase reactions, surface-based chemistry on grains, and photochemical processes. By incorporating the newly derived effective rate coefficients (ERCs) presented herein into such models, the potential for enhancing our comprehension of space chemistry is substantial. This integration not only facilitates an improved grasp of the chemical intricacies shaping the ISM but also paves the way for investigating its chemical evolution under diverse conditions, encompassing variable radiation fields, temperatures, and densities (e.g. Cuppen et al. 2017; Eistrup & Henning 2022, Rocha et al. 2023). It is worth noting that current calculations solve a coupled system of chemical reactions as a whole therefore proving values more realistic for solid-phase chemistry than if they were derived in gas-phase calculations or experiments.

Additionally, the intricate nature of ices undergoing radiation exposure in cosmic environments, particularly within protostellar ices, necessitates a chemical modelling approach that effectively integrates radiative transfer dynamics and reaction kinetics across both gas and solid phases. The outcomes derived from this investigation hold the potential to furnish invaluable insights for advancing such comprehensive modelling endeavours. Recent investigations, exemplified by studies like Ballering et al. (2021) and Rocha et al. (2023), have underscored the pivotal role of such integrated

modelling in unraveling the nuanced chemical evolution of ices within cosmic realms. Thus, the insights from this study are set to significantly enhance ongoing research, deepening our understanding of complex universal chemistry.

The desorption processes and numerical values from our experimental-computational research aid in comprehending the observed molecular abundances in gas-phase regions enriched with astrophysical ices. Notably emphasized by Lee et al. (2019), Öberg et al. (2021), and Sewiło et al. (2018), the presence of gaseous Complex Organic Molecules (COMs) in cold space regions, like protostellar clouds, aligns with solid-phase chemistry, offering insight into ice composition relevant to planet formation. Integrating our desorption rates and yields with radio wavelength observations, such as those from the Atacama Large Millimeter/submillimeter Array (ALMA), elucidates solid-gas interactions within cold astrophysical environments. Moreover, the temperature influence at the desorption of irradiated ices, releasing in different abundances to gas-phase depending on the ice temperature might also help us to clarify the amount of incoming radiation (mainly cosmic rays and X-rays) that reached embedded ices in dense and obscured clouds. The relationship between molecular desorption and the incoming radiation on astrophysical ices was discussed, for example, by Pilling et al. (2019) and Carvalho et al. (2024).

In summary, investigating irradiated astrophysical ices, with a focus on CO molecules, is crucial for comprehending interstellar medium chemistry and the relation between solid-phase chemistry with gas-phase chemistry in such environments. These insights not only shed light on organic compound origins but also aid ongoing research in astrochemistry and astrophysics.

5. CONCLUSION

In this paper, we present an experimental and theoretical investigation on the effect of the temperature (between 10 and 20 K) during the chemical evolution of irradiated CO ices by cosmic-ray analogues. The experimental data were obtained at GANIL laboratory at Caen, France. The samples were monitored by infrared spectroscopy during irradiation and the column densities of the several observed species were quantified. The computational analysis was performed by employing the PROCODA code to map the chemical evolution and kinetics of the irradiated samples. The current model incorporated 18 chemical species – 8 observed (CO, CO_2, C_3, O_3, C_2O, C_3O, C_3O_2, and C_5O_3) and 10 non-observed but predicted (C, O, C_2, O_2, CO_3, C_4O, C_5O, C_2O_2, C_2O_3, C_4O_2) – and a reaction network containing 156 reaction routes (including radiation-induced destruction reactions, bimolecular reactions, and desorption reactions). A comparison with the previous model was also performed. The main conclusions of this paper were:

I) Non-observed molecules and ERCs: Besides the determination of column densities of observed species and non-observed species (predicted), the best-fitting model provides the ERCs for 156 reaction routes indicating that temperature indeed affects their values. The average values of ERCs for intrinsic desorption and direct dissociation reactions have increased with the temperature. No clear dependence with temperature was observed for the bimolecular ERCs among the models errors.

II) Molecular abundances: Current models characterize more accurately the chemical equilibrium phase considering both observed and non-observed species in the experiments. At the chemical equilibrium, for all samples, the most produced species was atomic oxygen (>50 per cent) followed by atomic carbon (>15 per cent). The other important species at chemical equilibrium were CO (5–22 per cent), CO_2 (∼0.5–1 per cent), and CO_3 (∼0.05–0.1 per cent). The ice temperature affects the abundance of most species, including, for example, CO, CO_2, C_2O, and CO_3, which increases as *function* of the temperature. However, in the case of some species, for example, C, C_3, O_2, C_5O, and C_4O_2 we observed the opposite behaviour, a decrease in molecular abundance with the temperature enhancement. The abundances of frozen molecules, provided by this study, may help us to understand the detailed chemical abundances observed by modern space telescopes such as the *JWST*.

III) Difficulty to map the C_5O_2 evolution: As also observed in previously (Pilling et al. 2023a) the current model fails in the mapping of C_5O_2 data, yielding much lower abundances than observed in the experiment. Once more, we suggest that this discrepancy could be due to a combination of factors, such as a restricted number of reactions considered in the model, and/or an imprecise determination of the abundance of C_5O_2 in the experimental data.

IV) Thermochemistry behaviour of coupled solid-phase reactions: The results indicated changes in the thermochemical behaviour observed for some reactions comparing both gas- and ice-phase are probably related to the presence of the surrounding molecules. For example, in the case of ice-phase reactions, the presence of neighbour species close to the reactants and the chemically coupling system itself increases the complexity and the interdependence of the reaction parameters. We expect this issue might be deepened and clarified in future researches.

V) Desorption processes: The best-fitting models have shown that the average radiation-induced desorption rate increases with the temperature. However individual changes were also detected. For example, for some species the desorption was correlated with the temperature (e.g. O, CO_2, O_3, C_3O, C_2O_2, CO_3, and C_2O_3) and for others was anticorrelated (e.g. C, C_2, CO, C_3, C_2O, C_4O, C_5O, C_4O_2, and C_5O_2). The atomic carbon and oxygen represent the most desorbed species. The desorption yield provided by this study helps us to understand the chemical abundances observed by radiotelescopes such as the ALMA.

This study offers crucial insights into the chemical evolution of CO-enriched ices under radiation, vital to solid-state astrochemistry. It illuminates the influence of temperature on the production and desorption of C-bearing molecules in the studied ices and clarifies the formation of extensive carbon-chain molecules in the interstellar medium, pivotal as precursors to complex organic compounds and potential life-building blocks. The ERCs provided in this paper, when applied to astrochemical models, might help us to explain some of the observed molecular species and their abundances, as well as the mechanisms behind their formation and desorption to gas phase. These findings deepen our understanding of interstellar medium chemistry as well as the effect of temperature on frozen ices exposed to ionizing radiation.

ACKNOWLEDGEMENTS

The authors acknowledge the Brazilian research agencies Conselho Nacional de Desenvolvimento Científico e Tecnológico – CNPq (#302985/2018–2; #302939/2022–9; #302608/2022–2; #313624/2019–4; #407124/2022–5), FAPESP and Coordenação de Aperfeiçoamento de Pessoal de Nível Superior – CAPES (#PDPG/88887.691437/2022–00).

DATA AVAILABILITY

The data underlying this article will be shared on reasonable request to the corresponding author.

REFERENCES

Almeida G. C., Pilling S., De Barros A. L. F., Da Costa C. A. P., Pereira R. C., Da Silveira E. F., 2017, MNRAS, 471, 1330
Alves E., Franco M. P., Pilling S., Machado F. B., Spada R. F., 2021, J. Mol. Model., 27, 1
Andrade D. P., de Barros A. L., Pilling S., Domaracka A., Rothard H., Boduch P., Silveira da, 2013, MNRAS, 430, 787
Arrhenius S., 1889, Z. Phys. Chem., 4, 96
Atkins P., de Paula J., Keeler J. 2018, Atkins' Physical Chemistry 11e: Volume 1: Thermodynamics and Kinetics 11th Edition. Oxford Univ. Press. Oxford
Augé B., Been T., Boduch P., Chabot M., Dartois E., Madi T., Voivenel P., 2018, Rev. Sci. Instrum., 89, 075105
Ballering N. P., Cleeves L. I., Anderson D. E., 2021, ApJ, 920, 115
Bennett C. J., Kaiser R. I., 2005, ApJ, 635, 1362
Bergantini A., Pilling S., Nair B. G., Mason N. J., Fraser H. J., 2014a, A&A, 570, A120
Bergantini A., Pilling S., Rothard H., Boduch P., Andrade D. P. P., 2014b, MNRAS, 437, 2720
Berné O. et al., 2023, Nature, 621, 56
Bertrand T., Forget F., 2016, Nature, 540, 86
Boduch P. et al., 2011, Adv. Astron., 2011, 327641
Boduch P. et al., 2015, J. Phys. Conf. Ser., 629, 012008
Bonfim V. S., de Castilho R. B., Baptista L., Pilling S., 2017, Phys. Chem. Chem. Phys., 19, 26906
Boogert A. C. A., Gerakines P. A., Whittet D. C. B., 2015, ARA&A, 53, 541
Brown W. L., Augustyniak W. M., Marcantonio K. J., Simmons E. H., Boring J. W., Johnson R. E., Reimann C. T., 1984, Nucl. Instrum. Meth. Phys. Res. B, 1, 307
Carvalho G. A., Pilling S., Galvão B. R., 2022, MNRAS, 515, 3760
Carvalho G. A., Pilling S., Gerasimenko S., 2024, MNRAS, 527, 2781
Cernicharo J., Goicoechea J. R, Caux E. 2000, ApJ, 534, L199
Ciaravella A. et al., 2012, ApJ, 746, L1
Ciaravella A. et al., 2016, ApJ, 819, 38
Collings M. P., Anderson M. A., Chen R., Dever J. W., Viti S., Williams D. A., McCoustra M. R., 2004, MNRAS, 354, 1133
Cottin H., Moore M. H., Bénilan Y., 2003, ApJ, 590, 874
Crovisier J., Encrenaz T., Combes M. 1991, Nature, 353, 610
Cuppen H. M., Walsh C., Lamberts T., Semenov D., Garrod R. T., Penteado E. M., Ioppolo S., 2017, Space Sci. Rev., 212, 1
Dartois E. et al., 2019, A&A, 627, A55
Dartois E., Chabot M., Bacmann A., Boduch P., Domaracka A., Rothard H., 2020, A&A, 634, A103
Dartois E., Chabot M., Barkach T. I., Rothard H., Boduch P., Augé B., Agnihotri A. N., 2021, A&A, 647, A177
De Barros A. L. F. et al., 2011, Nucl. Instrum. Methods Phys. Res. B, 269, 852
De Barros A. L. F., Da Silveira E. F., Pilling S., Domaracka A., Rothard H., Boduch P., 2014, MNRAS, 438, 2026
De Barros A. L. F. et al., 2020, MNRAS, 499, 2162
De Barros A. L. F. et al., 2022, MNRAS, 511, 2491
d'Hendecourt L. B., Allamandola L. J., 1986, A&ASS, 64, 453
Domaracka A. et al. 2009, in Cunha K., Spite M., Barbuy B., eds, Proc. IAU Symp. S265, Chemical Abundances in the Universe: Connecting First Stars to Planets. Cambridge Univ. Press, Cambridge, p. 428
Domaracka A. et al. 2010, Nucl. Instrum. Methods Phys. Res. B, 268, 2960
Eistrup C., Henning T. 2022, A&A, 667, A160
Famá M., Shi J., Baragiola R. A., 2008, Surface Sci., 602, 156
Freitas F. M., Pilling S., 2020, Quim. Nova, 43, 521
Gerakines P. A., Schutte W. A., Greenberg J. M., van Dishoeck E. F., 1995, A&A, 296, 810
Gerakines P. A., Moore M. H., 2001, Icarus, 154, 372
Gerakines P. A., Materese C. K., Hudson R. L., 2023, MNRAS, 522, 3145
Gibb E. L., Whittet D. C. B., Boogert A. C. A., Tielens A. G. G. M., 2004, ApJS, 151, 35
Heays A. N., Bosman A. V., Van Dishoeck E. F., 2017, A&A, 602, A105
Herbst E., van Dishoeck E. F., 2009, ARA&A, 47, 427
Huntress W. T., Allen M., Delitsky M., 1991, Nature, 352, 316
Huang C. H. et al., 2020, ApJ, 889, 57
Ivlev A. V. et al., 2023, ApJl, 944, 181
Jamieson C. S., Mebel A. M., Kaiser R. I., 2006, ApJSS, 163, 184
Laidler K. J., 1984, J. Chem. Educ., 61, 494
Lee J. E. et al., 2019, Nat. Astron., 3, 314
Lellouch E., de Bergh C., Sicardy B., Ferron S., Käuf H.-U., 2010, A&A, 518, L8
Loeffler M. J., Baratta G. A., Palumbo M. E., Strazzulla G., Baragiola R. A., 2005, A&A, 435, 587
Lv X. Y. et al., 2012, A&A, 546, A81
McClure M. K. et al., 2023, Nat. Astron., 7, 431
Mennella V., Baratta G. A., Esposito A., Ferini G., Pendleton Y. J., 2003, ApJ, 587, 727
Mills I., Cvitas T., Homann K., Kallay N., Kuchitsu K.,1993, Quantities, Units and Symbols in Physical Chemistry, 2nd edn. Blackwell Science Ltd., Oxford. Available at: https://goldbook.iupac.org/files/pdf/green_book_2ed.pdf
Mookerjea B. et al., 2010, A&A, 521, L13
Nastasi M., Mayer J., Hirvonen J. K., 1996, Ion-Solid Interactions: Fundamentals and Applications, Cambridge Solid State Science Series. Cambridge Univ. Press, Cambridge
Öberg K. I. et al., 2011, ApJ, 740, 109
Öberg K. I. et al., 2021, ApJSS, 257, 1
Ohishi M. et al. 1991, ApJ, 380, L39
Paiva M. A., Pilling S., Mendoza E., Galvão B. R., De Abreu H. A., 2023, MNRAS, 519, 2518
Palumbo M. E., Leto P., Siringo C., Trigilio C., 2008, ApJ, 685, 1033
Pilling S., Andrade D. P., Neto A. C., Rittner R., Naves de Brito A., 2009, J. Phys. Chem. A, 113, 11161
Pilling S., Duarte E. S., Da Silveira E. F., Balanzat E., Rothard H., Domaracka A., Boduch P., 2010a, A&A, 509, A87
Pilling S., Duarte E. S., Domaracka A., Rothard H., Boduch P., Da Silveira E. F., 2010b, A&A, 523, A77
Pilling S., Duarte E. S., Domaracka A., Rothard H., Boduch P., Da Silveira E. F., 2011a, Phys. Chem. Chem. Phys., 13, 15755
Pilling S. et al., 2011b, MNRAS, 411, 2214
Pilling S., Andrade D. P. P., Da Silveira E. F., Rothard H., Domaracka A., Boduch P., 2012, MNRAS, 423, 2209
Pilling S., Mendes L. A., Bordalo V., Guaman C. F., Ponciano C. R., da Silveira E. F., 2013, Astrobiology, 13, 79
Pilling S., Bergantini A., 2015, ApJ, 811, 151
Pilling S., Rocha W. R. M., Freitas F. M., Da Silva P. A., 2019, RSC Adv., 9, 28823
Pilling S., Bonfim V. S., 2020, RSC Adv., 10, 5328
Pilling S., Pazianotto M. T., de Souza L. A., 2021, ApJ, 921, 116
Pilling S., Carvalho G. A., Rocha W. R., 2022a, ApJ, 925, 147
Pilling S., Pazianotto M. T., de Souza L. A., Maciel do Nascimento L., 2022b, MNRAS, 509, 6169
Pilling S., Carvalho G. A., de Abreu H. A., Galvão B. R. L., da Silveira C. H., Mateus M. S., 2023a, ApJ, 952, 17
Pilling S., Rocha W. R., Carvalho G. A., de Abreu H. A., 2023b, Adv. Space Res., 71, 5466
Pilling S., da Silveira C. H., Ojeda-Gonzalez A., 2023c, MNRAS, 523, 2858
Portugal W., Pilling S., Boduch P., Rothard H., Andrade D. P., 2014, MNRAS, 441, 3209
Rachid M. G., Pilling S., Rocha W. R. M., Agnihotri A., Rothard H., Boduch P., 2020, MNRAS, 494, 2396
Roberts J. F. et al., 2007, MNRAS, 382, 733
Rocha W. R. M. et al., 2023, A&A, 673, A70
Seperuelo-Duarte E. et al., 2009, A&A, 502, 599
Seperuelo-Duarte E. S., Domaracka A., Boduch P., Rothard H., Dartois E., Da Silveira E. F., 2010, A&A, 512, A71

Sewiło M. et al., 2018, ApJ, 853, L19
Spilker J. S. et al., 2023, Nature, 618, 708
Soustelle M., 2011, An Introduction to Chemical Kinetics, John Wiley & Sons, Inc., Hoboken, NJ
Souza S. P., Lutz B. L., 1977, ApJ, 216, L49
Steinfeld J. L., Francisco J. S., Hase W. L., 1998, Chemical Kinetics and Dynamics, 2nd edn. Pearson, London
Tarafdar S. P., 1992, in Singh P.D., eds, Proc. IAU Symp. 150, Astrochemistry of Cosmic Phenomena. Cambridge Univ. Press. Cambridge, p. 55
Van ´t Hoff J. H., 1884, Etudes De Dynamique Chimique. Kessinger Publishing, LLC, Montana, USA
Vasconcelos F. A., Pilling S., Rocha W. R. M., Rothard H., Boduch P., Ding J. J., 2017a, Phys. Chem. Chem. Phys., 19, 12845
Vasconcelos F. A., Pilling S., Rocha W. R. M., Rothard H., Boduch P., 2017b, Phys. Chem. Chem. Phys., 19, 24154
Vasconcelos F. D. A., Pilling S., Rocha W. R., Rothard H., Boduch P., 2017c, ApJ, 850, 174
Vasconcelos F. A., Pilling S., Agnihotri A., Rothard H., Boduch P., 2020, Icarus, 351, 113944
Whittet D. C. B. et al., 1998, ApJ, 498, L159
Ziegler J. F., Ziegler M. D., Biersack J. P., 2010, Nucl. Instrum. Methods Phys. Res. B, 268, 1818

APPENDIX A: COMPARISON BETWEEN HEAVY AND LIGHT COSMIC RAYSFIGU

Figure A1 presetns selected ion properties during bombardment with CO ices for proton, Ni, Fe, and Xe ions as a function of ion energy/mass calculated by SRIM code (Ziegler et al. 2010). Panel (a) details the linear energy deposition, or dEdx (also known as Stopping Power), measured in keV μm^{-1}. It illustrates the energy deposition within the nuclear and electronic domains of stopping power, represented by dashed and solid lines, respectively. For an in-depth understanding of stopping power, refer to Ivlev et al. (2023), who have extensively explored the microscopic mechanisms governing radiolysis and sputtering in astrophysical ices subjected to cosmic-ray ion bombardment in both domains. For a comprehensive discourse on the interactions between heavy and light ions with CO ices, consult Seperuelo-Duarte et al. (2010) and also Brown et al. (1984). Panel (b) displays the penetration depth of the selected ions in CO ice, in μm. Arrows indicate the conditions pertinent to both the current and previous experiments, the latter being the work of Seperuelo-Duarte et al. (2010), as included in the study by Pilling et al. (2023a) which also utilized the PROCODA code.

Calculations from the SRIM code reveal that the electronic domain's energy deposition, dEdx, for 50 MeV $^{58}Ni^{13+}$ ions (0.86 MeV u^{-1}) is 2900 keV μm^{-1}, while for 95.2 MeV $^{136}Xe^{23+}$ ions (0.7 MeV u^{-1}), it is approximately 5000 keV μm^{-1}. This indicates that the latter is about 1.7 times more energetic. Moreover, the penetration depths for both ions in CO ices are estimated to be around 30 μm. These figures suggest that the effects caused by Xe ions are comparable to those by 50 MeV Ni and also Fe ions within the electronic domain of stopping power. However, a greater desorption is anticipated for Xe ions, as the sputtering yield is proportional to the square of the electronic stopping power (refer to discussions in Seperuelo-Duarte et al. 2010, and Brown et al. 1984). This paper records higher desorption values induced by Xe ions compared to Ni ions (previous work), aligning with expectations.

APPENDIX B: THERMOCHEMISTRY BEHAVIOUR OF SOLID PHASE STUDIED REACTION PAIRS DERIVED BY A METHODOLOGY EMPLOYING THE VAN´T HOFF EQUATION

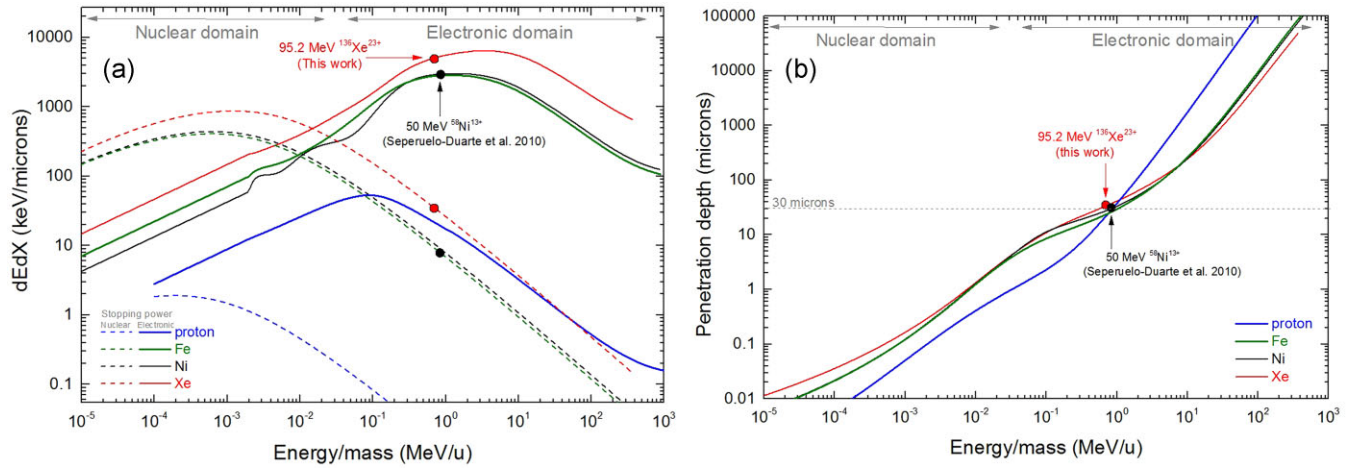

Figure A1 Selected ion properties during bombardment with CO ices for proton, Ni, Fe, and Xe ions as a function of ion energy/mass calculated by SRIM code (Ziegler et al. 2010) Panel (a) presents the linear energy deposition or dEdx (also named Stopping Power) in units of keV μm^{-1}. Dashed lines show the energy deposition within the nuclear domain of stopping power and solid lines within the electronic domain. Panel (b) presents the penetration depth of the selected projectiles within the CO ice, in units of μm. Arrows show the conditions of the current experiment and the previous experiment of Seperuelo-Duarte et al. (2010) considered in the work of Pilling et al. (2023a) also employing the PROCODA code.

Table B1. The studied reaction pairs and their thermochemistry behaviour suggested for the ice-phase derived by employing Van´t Hoff equation methodology. For comparison purposes the reaction enthalpy and its thermochemistry behaviour for the single reactions at gas phase (employed in phase 1 calculations of PROCODA) are listed.

Forward reactions					Reverse reactions				
Label	Reactants	Products	Thermochemistry behaviour at ice phase (considering Van't Hoff equation)*	Thermochemistry behaviour at gas phase ($\Delta_r H^o$ in kJ mol^{-1}) (employed in phase 1 calculation)	Label	Reactants**	Products	Thermochemistry behaviour at ice phase (considering Van ´t Hoff equation)*	Thermochemistry behaviour at gas phase ($\Delta_r H^o$ in kJ mol^{-1}) (employed in phase 1 calculation)
r1	CO2 + RAD	O + CO	ENDOTHERMIC	ENDOTHERMIC [526.15]	r2	O + CO	CO2	EXOTHERMIC	EXOTHERMIC [-526.15]
r3	CO2 + RAD	C + O2	EXOTERMIC	ENDOTHERMIC [1104.5]	r4	C + O2	CO2	ENDOTHERMIC	EXOTHERMIC [-1104.5]
r5	CO2 + CO2	O2 + C2O2	EXOTHERMIC	ENDOTHERMIC [801.12]	r6	O2 + C2O2	CO2 + CO2	ENDOTHERMIC	EXOTHERMIC [-801.12]
r7	CO2 + CO2	O + C2O3	EXOTHERMIC	ENDOTHERMIC [750.86]	r8	O + C2O3	CO2 + CO2	ENDOTHERMIC	EXOTHERMIC [-750.86]
r9	CO2 + CO2	CO + CO3	ENDOTHERMIC	ENDOTHERMIC [545.49]	r10	CO + CO3	CO2 + CO2	EXOTHERMIC	EXOTHERMIC [-545.49]
r11	O + CO2	CO + O2	ENDOTHERMIC	ENDOTHERMIC [32.47]	r12	CO + O2	O + CO2	EXOTHERMIC	EXOTHERMIC [-32.47]
r13	O + CO2	C + O3	?	ENDOTHERMIC [1002.05]	r14	C + O3	O + CO2	?	EXOTHERMIC [-1002.05]
r15	O + CO2	CO3	ENDOTHERMIC	ENDOTHERMIC [19.34]	r16		O + CO2	EXOTHERMIC	EXOTHERMIC [-19.34]
						CO3 + RAD			
r17	O2 + CO2	CO + O3	ENDOTHERMIC	ENDOTHERMIC [423.7]	r18	CO + O3	O2 + CO2	EXOTHERMIC	EXOTHERMIC [-423.7]
r19	O2 + CO2	O + CO3	ENDOTHERMIC	ENDOTHERMIC [513.02]	r20	O + CO3	O2 + CO2	EXOTHERMIC	EXOTHERMIC [-513.02]
r21	C + CO2	C2 + O2	EXOTHERMIC	ENDOTHERMIC [502.05]	r22	C2 + O2	C + CO2	ENDOTHERMIC	EXOTHERMIC [-502.05]
r23	C + CO2	CO + CO	ENDOTHERMIC	EXOTHERMIC [-545.8]	r24	CO + CO	C + CO2	EXOTHERMIC	ENDOTHERMIC [545.8]
r25	C + CO2	C2O2	EXOTHERMIC	EXOTHERMIC [-303.38]	r26		C + CO2	ENDOTHERMIC	ENDOTHERMIC [303.38]
						C2O2 + RAD			
r27	CO + CO2	C2O3	ENDOTHERMIC	ENDOTHERMIC [224.71]	r28		CO + CO2	EXOTHERMIC	EXOTHERMIC [-224.71]
						C2O3 + RAD			
r29	CO + CO2	O + C2O2	EXOTHERMIC	ENDOTHERMIC [768.65]	r30	O + C2O2	CO + CO2	ENDOTHERMIC	EXOTHERMIC [-768.65]
r31	CO + CO2	O2 + C2O	ENDOTHERMIC	ENDOTHERMIC [884.03]	r32	O2 + C2O	CO + CO2	EXOTHERMIC	EXOTHERMIC [-884.03]
r33	CO + CO2	C2 + O3	ENDOTHERMIC	ENDOTHERMIC [1471.63]	r34	C2 + O3	CO + CO2	EXOTHERMIC	EXOTHERMIC [-1471.63]
r35	C2O + CO2	CO + C2O2	EXOTHERMIC	EXOTHERMIC [-82.91]	r36	CO + C2O2	C2O + CO2	ENDOTHERMIC	ENDOTHERMIC [82.91]
r37	C2O + CO2	C + C2O3	EXOTHERMIC	ENDOTHERMIC [445.18]	r38	C + C2O3	C2O + CO2	ENDOTHERMIC	EXOTHERMIC [-445.18]
r39	C2 + CO2	CO + C2O	EXOTHERMIC	EXOTHERMIC [-163.9]	r40	CO + C2O	C2 + CO2	ENDOTHERMIC	ENDOTHERMIC [163.9]
r41	C2 + CO2	C + C2O2	EXOTHERMIC	ENDOTHERMIC [299.07]	r42	C + C2O2	C2 + CO2	ENDOTHERMIC	EXOTHERMIC [-299.07]
r43	CO2 + O3	O2 + CO3	EXOTHERMIC	ENDOTHERMIC [121.79]	r44	O2 + CO3	CO2 + O3	ENDOTHERMIC	EXOTHERMIC [-121.79]
r45	CO + RAD	C + O	?	ENDOTHERMIC [1072.03]	r46	C + O	CO	?	EXOTHERMIC [-1072.03]
r47	CO + CO	C2O2	ENDOTHERMIC	ENDOTHERMIC [242.5]	r48		CO + CO	EXOTHERMIC	EXOTHERMIC [-242.5]
						C2O2 + RAD			
r49	CO + CO	C2 + O2	EXOTHERMIC	ENDOTHERMIC [1047.93]	r50	C2 + O2	CO + CO	ENDOTHERMIC	EXOTHERMIC [-1047.93]
r51	CO + CO	O + C2O	ENDOTHERMIC	ENDOTHERMIC [851.56]	r52	O + C2O	CO + CO	EXOTHERMIC	EXOTHERMIC [-851.56]
r53	C + CO	C2O	EXOTHERMIC	EXOTHERMIC [-220.47]	r54		C + CO	ENDOTHERMIC	ENDOTHERMIC [220.47]
						C2O + RAD			
r55	C + CO	O + C2	EXOTHERMIC	ENDOTHERMIC [469.58]	r56	O + C2	C + CO	ENDOTHERMIC	EXOTHERMIC [-469.58]
r57	O + CO	C + O2	EXOTHERMIC	ENDOTHERMIC [578.35]	r58	C + O2	O + CO	ENDOTHERMIC	EXOTHERMIC [-578.35]
r59	C2 + CO	C + C2O	ENDOTHERMIC	ENDOTHERMIC [381.98]	r60	C + C2O	C2 + CO	EXOTHERMIC	EXOTHERMIC [-381.98]
r61	CO + C2O	C + C2O2	EXOTHERMIC	ENDOTHERMIC [462.97]	r62	C + C2O2	CO + C2O	ENDOTHERMIC	EXOTHERMIC [-462.97]
r63	CO + O2	C + O3	ENDOTHERMIC	ENDOTHERMIC [969.58]	r64	C + O3	CO + O2	EXOTHERMIC	EXOTHERMIC [-969.58]
r65	CO + O2	CO3	?	EXOTHERMIC [-13.13]	r66		CO + O2	?	ENDOTHERMIC [13.13]
						CO3 + RAD			
r67	CO + O3	O + CO3	ENDOTHERMIC	ENDOTHERMIC [89.32]	r68	O + CO3	CO + O3	EXOTHERMIC	EXOTHERMIC [-89.32]
r69	O2 + RAD	O + O	EXOTHERMIC	ENDOTHERMIC [493.68]	r70	O + O	O2	ENDOTHERMIC	EXOTHERMIC [-493.68]
r71	O3 + RAD	O + O2	?	ENDOTHERMIC [102.45]	r72	O + O2	O3	ENDOTHERMIC	EXOTHERMIC [-102.45]

Table B1 – *continued*

Forward reactions					Reverse reactions				
Label	Reactants	Products	Thermochemistry behaviour at ice phase (considering Van't Hoff equation)*	Thermochemistry behaviour at gas phase ($\Delta_r H^o$ in kJ mol^{-1}) (employed in phase 1 calculation)	Label	Reactants**	Products	Thermochemistry behaviour at ice phase (considering Van 't Hoff equation)*	Thermochemistry behaviour at gas phase ($\Delta_r H^o$ in kJ mol^{-1}) (employed in phase 1 calculation)
r73	C2 + RAD	C + C	EXOTHERMIC	ENDOTHERMIC [602.45]	r74	C + C	C2	ENDOTHERMIC	EXOTHERMIC [-602.45]
r75	C2O3 + RAD	O + C2O2	ENDOTHERMIC	ENDOTHERMIC [543.94]	r76	O + C2O2	C2O3	EXOTHERMIC	EXOTHERMIC [-543.94]
r77	C2O3 + RAD	O2 + C2O	EXOTHERMIC	ENDOTHERMIC [659.32]	r78	O2 + C2O	C2O3	ENDOTHERMIC	EXOTHERMIC [-659.32]
r79	C3 + RAD	C + C2	ENDOTHERMIC	ENDOTHERMIC [717.07]	r80	C + C2	C3	EXOTHERMIC	EXOTHERMIC [-717.07]
r81	C3O + RAD	C + C2O	EXOTHERMIC	ENDOTHERMIC [758.51]	r82	C + C2O	C3O	ENDOTHERMIC	EXOTHERMIC [-758.51]
r83	C3O + RAD	C2 + CO	EXOTHERMIC	ENDOTHERMIC [376.53]	r84	C2 + CO	C3O	ENDOTHERMIC	EXOTHERMIC [-376.53]
r85	C3O + RAD	O + C3	EXOTHERMIC	ENDOTHERMIC [731.49]	r86	O + C3	C3O	ENDOTHERMIC	EXOTHERMIC [-731.49]
r87	C3O2 + RAD	C + C2O2	EXOTHERMIC	ENDOTHERMIC [828.3]	r88	C + C2O2	C3O2	ENDOTHERMIC	EXOTHERMIC [-828.3]
r89	C3O2 + RAD	C2 + CO2	ENDOTHERMIC	ENDOTHERMIC [529.23]	r90	C2 + CO2	C3O2	EXOTHERMIC	EXOTHERMIC [-529.23]
r91	C3O2 + RAD	O + C3O	?	ENDOTHERMIC [678.85]	r92	O + C3O	C3O2	?	EXOTHERMIC [-678.85]
r93	C3O2 + RAD	O2 + C3	ENDOTHERMIC	ENDOTHERMIC [916.66]	r94	O2 + C3	C3O2	EXOTHERMIC	EXOTHERMIC [-916.66]
r95	C2O2 + RAD	O + C2O	ENDOTHERMIC	ENDOTHERMIC [609.06]	r96	O + C2O	C2O2	EXOTHERMIC	EXOTHERMIC [-609.06]
r97	C2O2 + RAD	C2 + O2	ENDOTHERMIC	ENDOTHERMIC [805.43]	r98	C2 + O2	C2O2	EXOTHERMIC	EXOTHERMIC [-805.43]
r99	C2O3 + RAD	C + CO3	EXOTHERMIC	ENDOTHERMIC [866.66]	r100	C + CO3	C2O3	ENDOTHERMIC	EXOTHERMIC [-866.66]
r101	C2O3 + RAD	C2 + O3	EXOTHERMIC	ENDOTHERMIC [1246.92]	r102	C2 + O3	C2O3	ENDOTHERMIC	EXOTHERMIC [-1246.92]
r103	C4O + RAD	C + C3O	?	ENDOTHERMIC [468.37]	r104	C + C3O	C4O	?	EXOTHERMIC [-468.37]
r105	C4O + RAD	C2 + C2O	ENDOTHERMIC	ENDOTHERMIC [624.43]	r106	C2 + C2O	C4O	EXOTHERMIC	EXOTHERMIC [-624.43]
r107	C4O + RAD	CO + C3	ENDOTHERMIC	ENDOTHERMIC [127.83]	r108	CO + C3	C4O	EXOTHERMIC	EXOTHERMIC [-127.83]
r109	C4O2 + RAD	C + C3O2	ENDOTHERMIC	ENDOTHERMIC [455.59]	r110	C + C3O2	C4O2	EXOTHERMIC	EXOTHERMIC [-455.59]
r111	C4O2 + RAD	C2 + C2O2	ENDOTHERMIC	ENDOTHERMIC [681.44]	r112	C2 + C2O2	C4O2	EXOTHERMIC	EXOTHERMIC [-681.44]
r113	C4O2 + RAD	C3 + CO2	ENDOTHERMIC	ENDOTHERMIC [267.75]	r114	C3 + CO2	C4O2	EXOTHERMIC	EXOTHERMIC [-267.75]
r115	C4O2 + RAD	CO + C3O	ENDOTHERMIC	ENDOTHERMIC [62.41]	r116	CO + C3O	C4O2	EXOTHERMIC	EXOTHERMIC [-62.41]
r117	C4O2 + RAD	O + C4O	ENDOTHERMIC	ENDOTHERMIC [666.07]	r118	O + C4O	C4O2	EXOTHERMIC	EXOTHERMIC [-666.07]
r119	C5O + RAD	C + C4O	ENDOTHERMIC	ENDOTHERMIC [696.89]	r120	C + C4O	C5O	EXOTHERMIC	EXOTHERMIC [-696.89]
r121	C5O + RAD	C2 + C3O	ENDOTHERMIC	ENDOTHERMIC [562.81]	r122	C2 + C3O	C5O	EXOTHERMIC	EXOTHERMIC [-562.81]
r123	C5O + RAD	C3 + C2O	ENDOTHERMIC	ENDOTHERMIC [604.25]	r124	C3 + C2O	C5O	EXOTHERMIC	EXOTHERMIC [-604.25]
r125	C5O2 + RAD	C + C4O2	ENDOTHERMIC	ENDOTHERMIC [713.14	r126	C + C4O2	C5O2	EXOTHERMIC	EXOTHERMIC [-713.14
r127	C5O2 + RAD	O + C5O	EXOTHERMIC	ENDOTHERMIC [682.32]	r128	O + C5O	C5O2	ENDOTHERMIC	EXOTHERMIC [-682.32]
r129	C5O2 + RAD	C2 + C3O2	ENDOTHERMIC	ENDOTHERMIC [566.28]	r130	C2 + C3O2	C5O2	EXOTHERMIC	EXOTHERMIC [566.28]
r131	C5O2 + RAD	C3 + C2O2	?	ENDOTHERMIC [677.51]	r132	C3 + C2O2	C5O2	?	EXOTHERMIC [-677.51]
r133	C5O2 + RAD	CO + C4O	EXOTHERMIC	ENDOTHERMIC [307.18]	r134	CO + C4O	C5O2	ENDOTHERMIC	EXOTHERMIC [-307.18]
r135	C5O2 + RAD	C2O + C3O	ENDOTHERMIC	ENDOTHERMIC [555.08]	r136	C2O + C3O	C5O2	EXOTHERMIC	EXOTHERMIC [-555.08]
r137	O2 + O2	O + O3	EXOTHERMIC	ENDOTHERMIC [391.23]	r138	O + O3	O2 + O2	ENDOTHERMIC	EXOTHERMIC [-391.23]

*Calculated considering the ERCs values at the temperatures of 10 K and 20 K; Reactions marked with '?' have presented small differences of $k_{for,Ti}/k_{bck,Ti}$ between the temperatures of 10 K and 20 K, and it was not suggested any thermochemistry behaviour due to eventual uncertainty in the methodology.

**These reactants were considered to be the products of the respective forward reactions.

This paper has been typeset from a Microsoft Word file prepared by the author.